Chapter 4

PHASE COMPOSITION, MICROSTRUCTURE, PHYSICAL AND MECHANICAL PROPERTIES

This chapter presents the results of phase and microstructural analysis, as well as measurements of density, porosity, hardness, and elastic modulus of the developed alloys. A comparative evaluation of these properties among the different alloy compositions is also provided, along with detailed discussions and justifications based on the observed trends.

4.1 Phase composition

4.1.1 X-ray diffraction analysis of ball-milled powders

4.1.1.1 XRD analysis of binary alloys powders

The binary alloys powders were ball-milled in a high energy planetary ball milling machine and the resulting powders were characterized by XRD. The patterns for both Ti-xNb and Ti-xZr binary alloys are shown in Fig. 4.1 and 4.2. In Fig. 4.1, XRD patterns of raw Ti, Nb, and ball-milled Ti-Nb powders are depicted. Examination of these patterns indicates the peaks of Ti and Nb powders correspond to known reference patterns (JCPDS Reference No: 00-044-1294 for Ti and 00-016-0001 for Nb). The Ti-Nb patterns display distinct Ti and Nb peaks, suggesting no oxidation or formation of intermetallic compounds due to the milling process in toluene wet medium and argon inert atmosphere. Moreover, as the amount of Nb content rises in ball-milled Ti-Nb powders, the intensity of Nb peaks rises, while Ti peaks decrease.

The pre-milling and post-milling XRD patterns of Ti and Zr powders are displayed in Fig. 4.2. The analysis of these patterns reveals that the elemental Ti and Zr powders utilized in this investigation exhibit no detectable impurities, as evidenced by the presence of distinct peaks matching with Ti (JCPDS Ref. No.: 00-044-1294) and Zr (01-089-3045) in their respective patterns. Moreover, the XRD patterns of the powders

post milling exhibit peaks that align exclusively with either Ti or Zr, corroborating the absence of oxides or undesired elements generated during the milling process. Thus, it can be inferred that no oxides or unwanted elements were produced during milling process. These results suggest, the controlled milling environment, using toluene as a process control agent and argon as an inert atmosphere, effectively suppresses oxidation and intermetallic formation during mechanical alloying of titanium-based systems. Similar observations have been reported in previous studies [174].

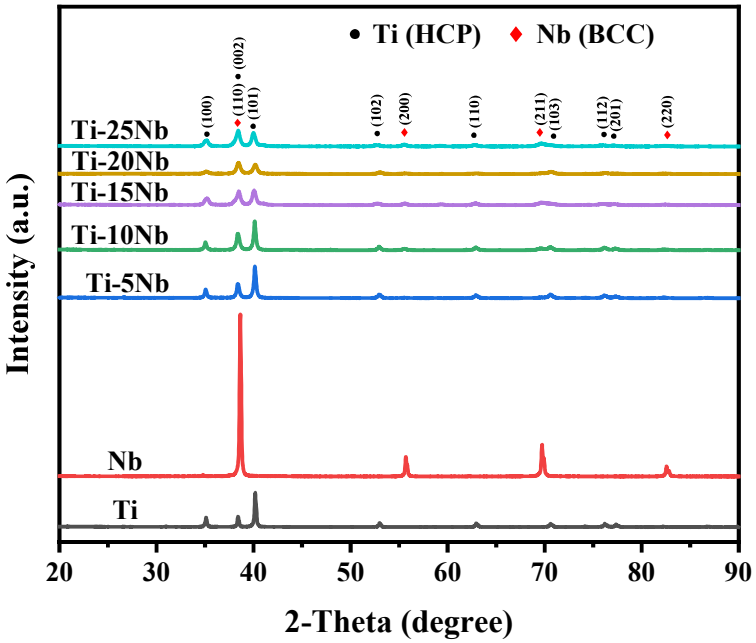

Fig. 4.1: XRD patterns of binary Ti powder, Nb powder, and Ti-xNb milled powders

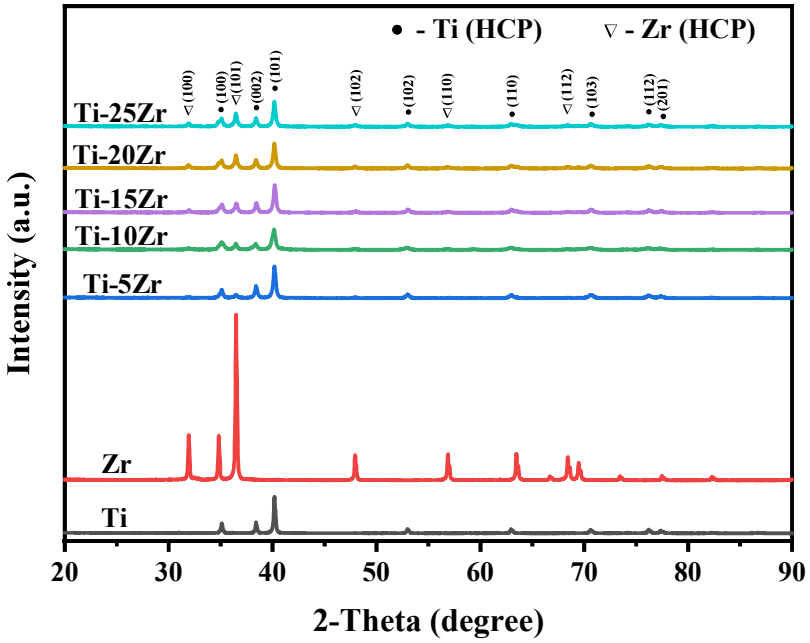

Fig. 4.2: XRD patterns of binary Ti powder, Zr powder, and Ti-xZr milled powders

4.1.1.2 XRD analysis of ternary alloys powders

Figure 4.3 shows the XRD patterns of Ti-10Zr and Ti-10Zr-xNb (x = 5, 10, 15, 20 wt.%) alloy powders synthesized through high-energy planetary ball milling. The Ti-10Zr binary alloy exhibits characteristic peaks corresponding to Ti and Zr, both of which are associated with a hexagonal close-packed (HCP) crystal structure, as confirmed by the Joint Committee on Powder Diffraction Standards (JCPDS) files for Ti (00-044-1294) and Zr (01-089-3045).

Upon the addition of Nb, new peaks appear in the XRD patterns that correspond to Nb with a body-centered cubic (BCC) structure (JCPDS 00-016-0001), indicating successful incorporation of Nb into the alloy system. The presence of distinct peaks of Ti, Zr, and Nb without any extra or shifted peaks suggests that no oxidation or intermetallic compounds formed during the milling process. With increasing Nb content, the intensity of BCC Nb peaks increases significantly, especially in the Ti-10Zr-20Nb composition, while the intensity of HCP Ti/Zr peaks gradually decreases.

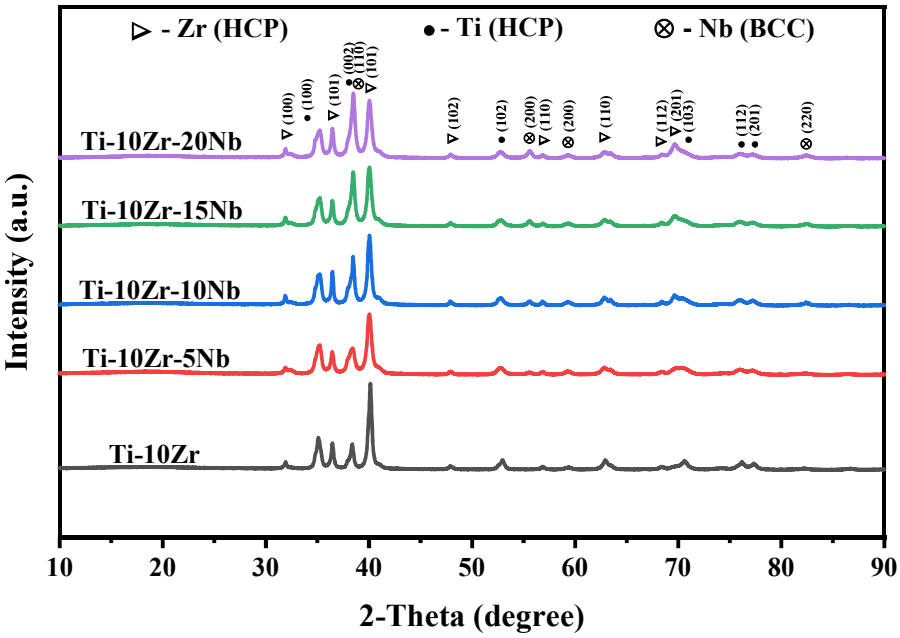

Fig. 4.3: XRD patterns of binary Ti-10Zr and Ti-10Zr-xNb milled powders

4.1.1.3 XRD analysis of high entropy alloys powders

The powders of five different elements for each high-entropy alloy composition were subjected to ball milling for 75 hours. The resulting powders after milling were characterized by XRD analysis. The XRD patterns are shown in Figs. 4.4 and 4.5. Figure 4.4 presents the patterns for $TiNb_{1.5}Mo_{1.1}Zr_{1.15}Cu_{0.25}$, while Fig. 4.5 shows those for $TiNbZr_{0.8}Mo_{0.92}Sn_{0.28}$ milled powders. At the initial milling stage (15 minutes), the peaks corresponding to the individual elements are clearly visible. With increasing milling duration, the intensity of these peaks decreases due to mechanical alloying. This decrease in intensity is accompanied by peak broadening, indicating a reduction in particle size and an increase in lattice strain [175]. For $TiNb_{1.5}Mo_{1.1}Zr_{1.15}Cu_{0.25}$ after 10 hours of milling minor peaks corresponding to Ti, Cu, and Zr disappeared, whereas other major peaks show a decrease in intensity and an increase in broadness. When a peak got disappeared that means some phases of the sample element either diminished or transformed into other phase. The element with lower melting point have tendency

to form solid solution early than high melting temperature element [176]. After 25 hours all the peaks of Cu disappeared, only peaks corresponding to Ti, Zr, and Mo remains also broadening of these peaks can be seen. Nb dissolves in Ti as from binary phase diagram it can be concluded that these elements formed a solid solution with each other [177]. After 35 hours, most of the elements lose their peaks, and some peaks of Zr also disappear. XRD of milling powder at 35 hours and 45 hours is almost same only a little peak broadening can be seen and it also ensured that a proper solid solution is formed. After 45 hours the $TiNb_{1.5}Mo_{1.1}Zr_{1.15}Cu_{0.25}$ consists of two phases one is BCC1 and another is BCC2. It also shows peaks of some undissolved Zr. The lattice parameters are 3.3044 Å for BCC1 and 3.1449 Å for BCC2. The BCC1 parameter is close to those of β-Ti (3.311 Å) and Nb (3.306 Å), indicating Ti and Nb as the host lattice, while BCC2 is close to Mo (3.15 Å), suggesting Mo as the host lattice.

For $TiNbZr_{0.8}Mo_{0.92}Sn_{0.28}$ after 5 hours some minor peaks of Sn got disappeared and intensity of major peaks decreases with increase in broadness. After 10 hours further Sn and some minor peaks of Mo got disappeared. After 25 hours Nb and Ti got dissolve in each other and after 35 hours most of the Sn peaks disappeared. At 50 hours of milling, the powder exhibited three phases: BCC1, BCC2, and HCP, with lattice parameters of 3.3044 Å, 3.1449 Å, and 3.572 Å, respectively. The BCC1 phase corresponds to Ti and Nb as the host lattice, BCC2 to Mo, and the HCP phase corresponds to Zr (lattice parameter ~3.61 Å).

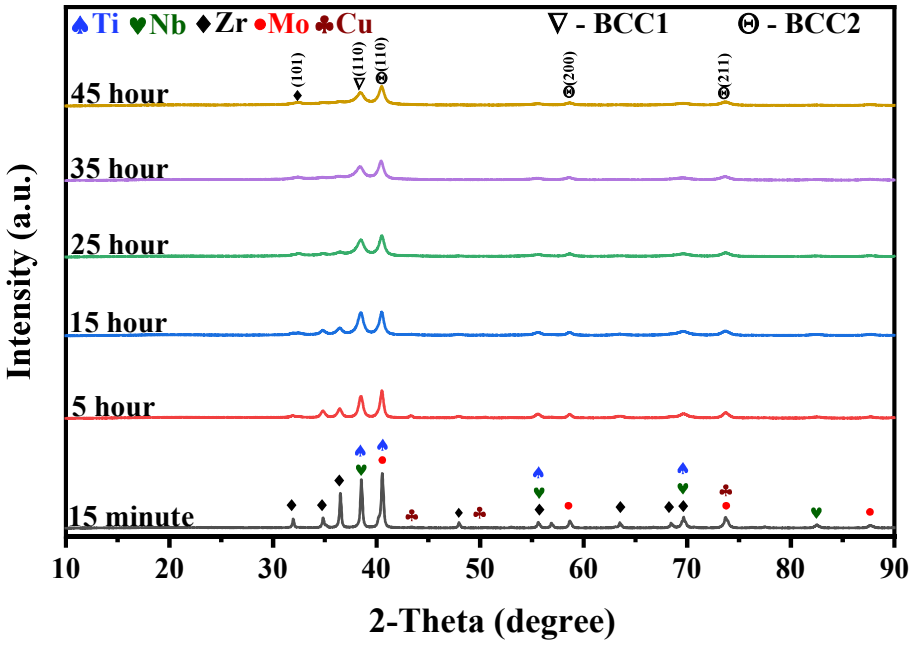

Fig. 4.4: XRD pattern of $TiNb_{1.5}Mo_{1.1}Zr_{1.15}Cu_{0.25}$ powder after milling

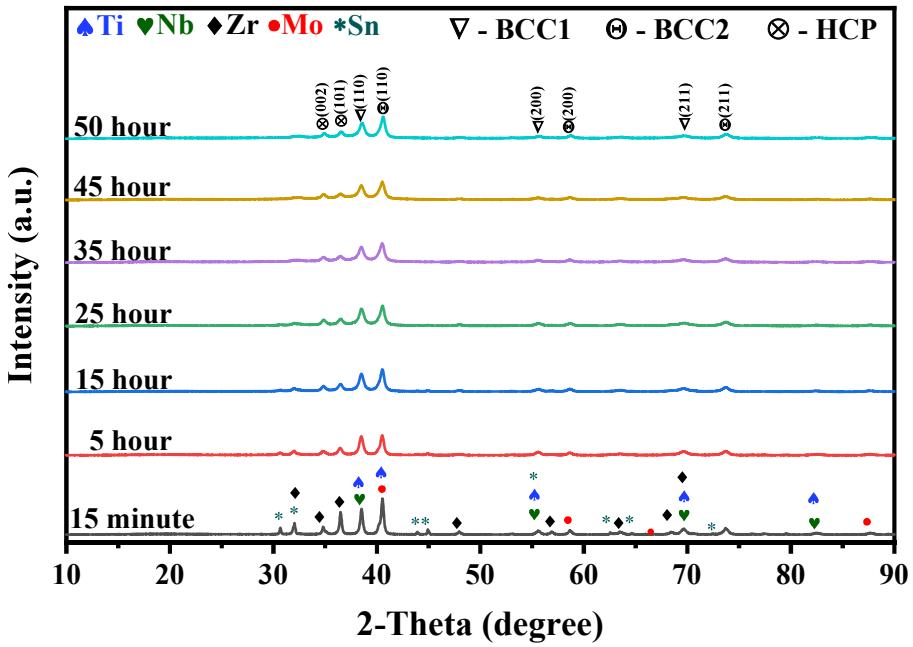

Fig. 4.5: XRD pattern of $TiNbZr_{0.8}Mo_{0.92}Sn_{0.28}$ powder after milling

4.1.2 X-ray diffraction analysis of cpTi, Ti-6Al-4V, and sintered alloys

4.1.2.1 XRD analysis of cpTi and Ti-6Al-4V

To compare the phase composition the XRD analysis of purchased cpTi and Ti-6Al-4V were conducted and the resulting XRD patterns are shown in Fig. 4.6. The XRD pattern of the cpTi revealed the presence of α-phase (HCP) as the predominant crystalline structure. Characteristic diffraction peaks corresponding to (100), (002), and (101) planes of α-Ti were observed at 2θ values of approximately 35°, 38°, and 40° respectively. This confirms the hexagonal crystal system typical for pure titanium at room temperature. The absence of secondary phases indicates that the cpTi retained its single-phase α-Ti microstructure, which is essential for its excellent corrosion resistance and moderate mechanical properties. The high-intensity peaks demonstrate a high degree of crystallinity, which is advantageous for biomedical applications requiring predictable material performance.

The XRD pattern of the Ti-6Al-4V alloy revealed a dual-phase microstructure comprising α-phase (HCP) and β-phase (BCC). The α-phase peaks correspond to planes (100), (002), and (101), similar to those observed in cpTi, while additional peaks at approximately 38° and 41° were indexed to the (011) and (101) planes of β-Ti. The presence of the β-phase is attributed to the alloying elements aluminium (Al) and vanadium (V). Aluminium stabilizes the α-phase, enhancing its mechanical strength and corrosion resistance, while vanadium is a β-phase stabilizer, improving the ductility and toughness of the alloy. The higher relative intensity of the α-phase peaks compared to the β-phase peaks indicates that α-phase is the dominant phase in the microstructure, consistent with the α + β design of Ti-6Al-4V.

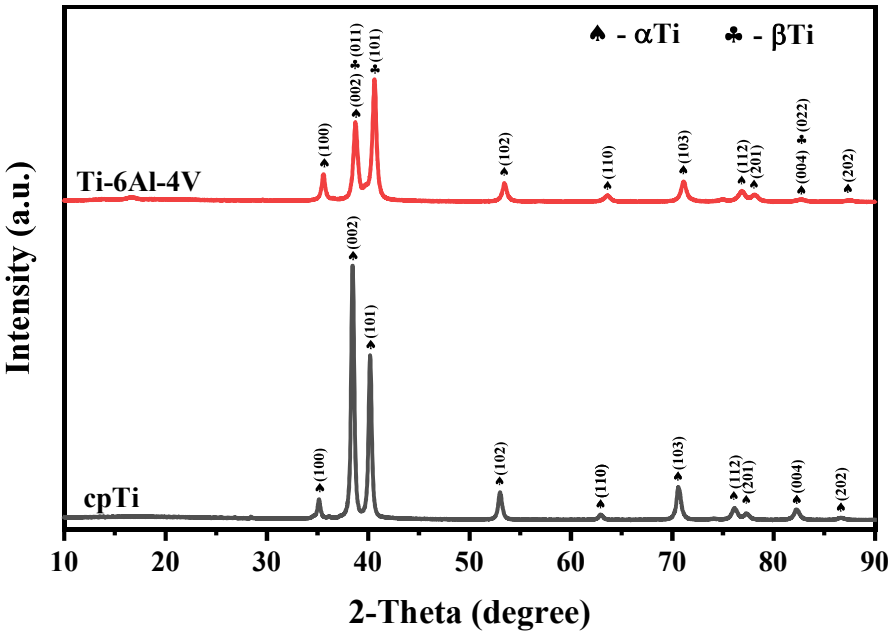

Fig. 4.6: XRD pattern of cpTi and Ti-6Al-4V

4.1.2.2 XRD analysis of sintered binary alloys

The sintered binary Ti-xNb alloys were characterized for phase composition using XRD analysis. The diffractograms obtained are shown in Fig. 4.7. This figure shows the XRD patterns of cpTi and Ti-Nb alloys. The cpTi exhibits the α phase, characterized by HCP structure. In contrast, the Ti-Nb alloys display a mixture of α and β phases, consisting of both HCP and BCC structures. Further analysis indicates that with increasing Nb content, the fraction of the β phase increases, while the intensity of the α phase peaks correspondingly decreases. The gradual increase in β phase fraction with Nb content aligns with the phase stability trends observed in Ti-Nb binary systems, where Nb promotes the formation of the BCC structure at higher concentrations [178].

Figure 4.8 displays the XRD patterns of the sintered Ti-xZr alloys. There is no presence of any secondary phase, according to the patterns, and only the α-phase with HCP structure is detected [179]. The presence of exclusively an α-phase throughout the developed alloys was justified by the comprehensive solid solution system displayed by Ti-Zr alloys [180]. Additionally, it was noted that when Zr concentration increased,

the peaks shifted to a lower angle. This is because Zr has a larger atomic radius (~1.62 Å) than Ti (~1.47 Å), which causes an increase in lattice parameters [181].

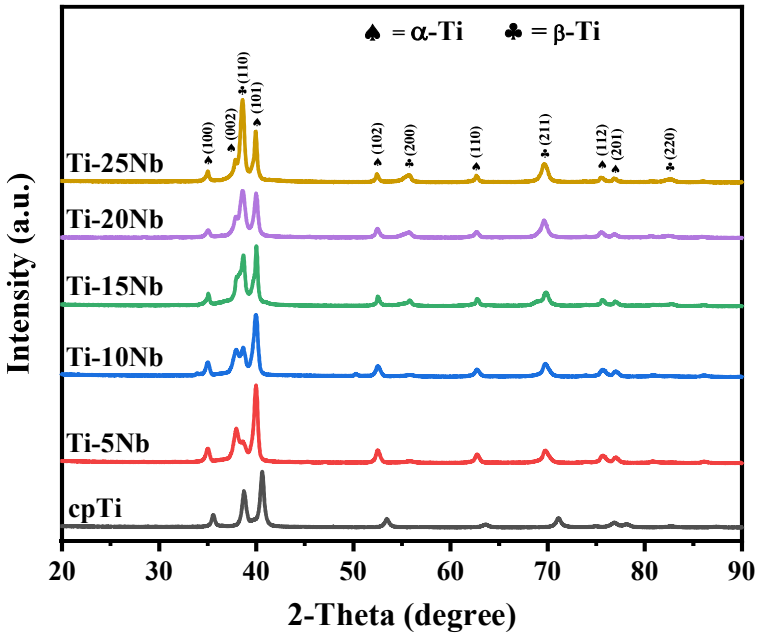

Fig. 4.7: XRD pattern of cpTi and sintered Ti-xNb alloys

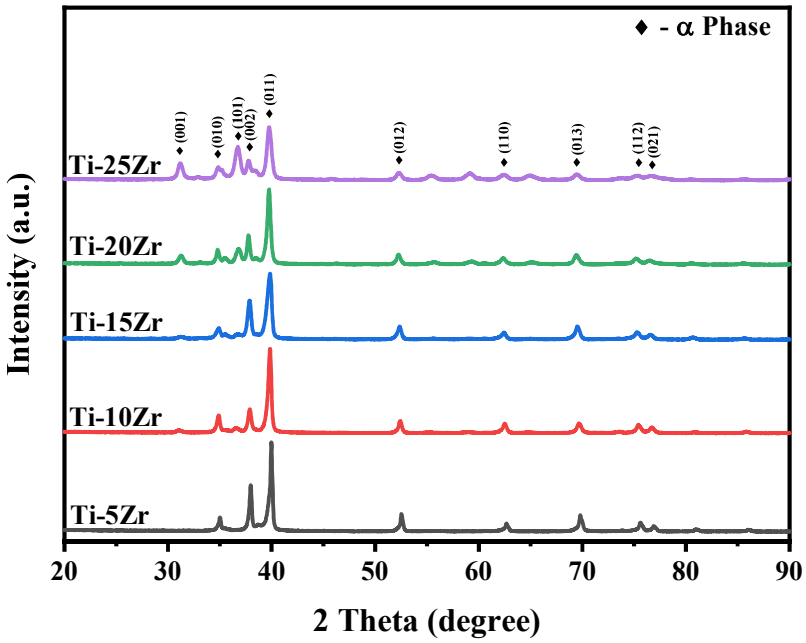

Fig. 4.8: XRD pattern of sintered Ti-xZr alloys

4.1.2.3 XRD analysis of sintered ternary alloys

The obtained XRD patterns for the Ti-10Zr-xNb (x = 5, 10, 15, 20 wt.%) alloys are shown in Fig. 4.9. The analysis confirmed the presence of both α-Ti and β-Ti phases in all the ternary alloys, indicating a mixture of HCP and BCC structures. In contrast, the Ti-10Zr binary alloy exhibited only the α-Ti phase. The addition of Nb resulted in slight peak shifts, confirming solid solution formation due to the substitution of Nb atoms into the Ti lattice. This shift is associated with the β-phase stabilizing nature of Nb, which is attributed to its electronic configuration and higher valence electron concentration. Variation in peak intensities with increasing Nb content suggests a compositional influence on phase stability [182,183]. Furthermore, the XRD patterns show no evidence of intermetallic compounds or secondary phases, indicating successful sintering of the alloys. The combined addition of Nb and Zr has been reported to suppress the β to α transformation in Ti alloys. Specifically, the presence of Zr reduces the critical Nb concentration required to retain the β phase at room temperature, thereby enhancing β-phase stability in Ti-Zr-Nb alloys [184,185].

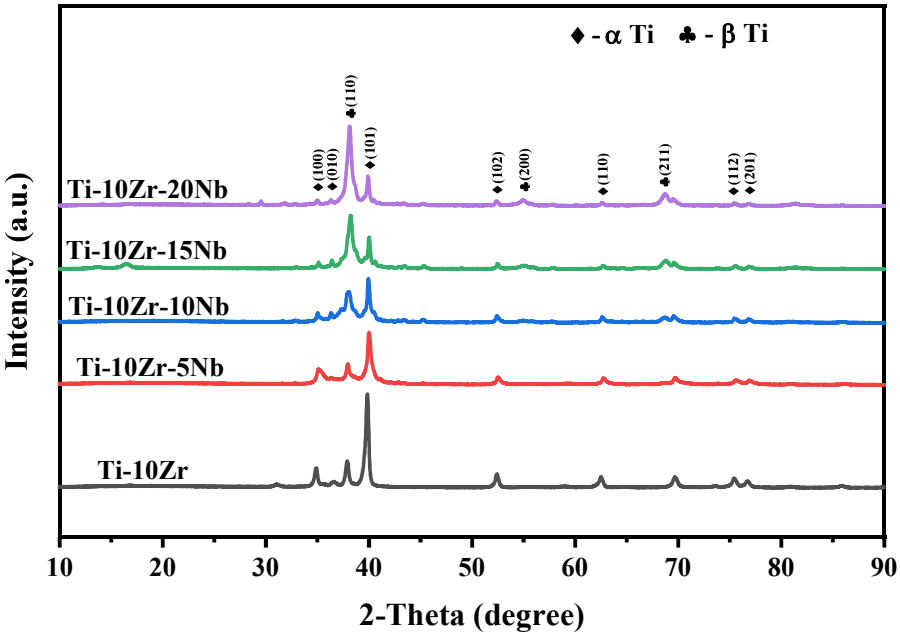

Fig. 4.9: XRD pattern of sintered Ti-10Zr and Ti-10Zr-xNb alloys

4.1.2.4 XRD analysis of sintered high entropy alloys

The XRD patterns for three different high entropy alloys are shown in Fig. 4.10 and 4.11. For $TiNb_{1.5}Mo_{1.1}Zr_{1.15}Cu_{0.25}$ have obtained BCC1, tetragonal, and orthorhombic phases. Some of the peaks show increased intensity after sintering which is due to grain coarsening and the release of internal stresses [186]. It can be seen that the peak intensity of BCC1 is more than other phases indicating a greater proportion of the BCC1 phase relative to other two phases. BCC2 phase and undissolved Zr undergoes phase transformation. We can see more peak intensity of XRD than milled powder at $2\theta =$ 49.5°, 56.38°, 65.84°, 78.10°, 84.22°. The formation of the tetragonal phase may have occurred from the orthorhombic phase which is due to the release of lattice stress [187]. The elevated temperature leads to reordering, which involves the formation of more stable phases than the initial metastable phases observed after mechanical alloying (MA) [188].

The $TiNbZr_{0.8}Mo_{0.92}Sn_{0.28}$ alloy exhibits three phases: BCC1, BCC2 and orthorhombic phase. It can be observed that the XRD pattern of the solid sample is almost identical to the XRD pattern obtained after milling. Additionally, there is a noticeable shift in the peak towards right side of the solid sample's XRD pattern. This may be because sintering can induce residual stresses in the crystal structure and compressive stresses can result in reduction of lattice parameter which causes the shift of peak towards higher angle [189]. It can also see the major HCP gets converted into orthorhombic phase with some extra intensity peaks at $2\theta = 29.58°$, 32.32° and 46.16°. The formation of the orthorhombic phase may be due to the induced residual stresses after sintering, which lead to a martensitic transformation and thus can be the main reason for development of orthorhombic phase [190].

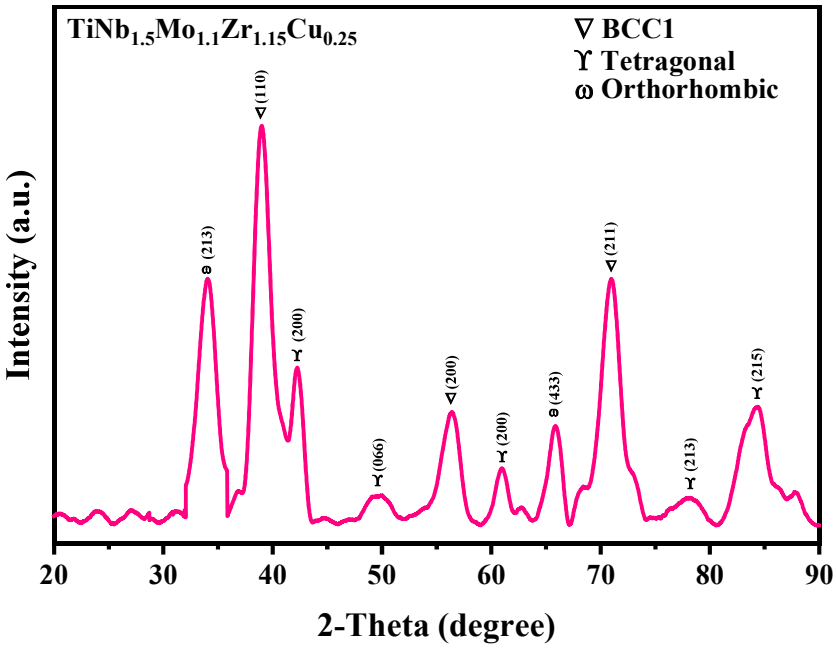

Fig. 4.10: XRD pattern of sintered $TiNb_{1.5}Mo_{1.1}Zr_{1.15}Cu_{0.25}$ HEA

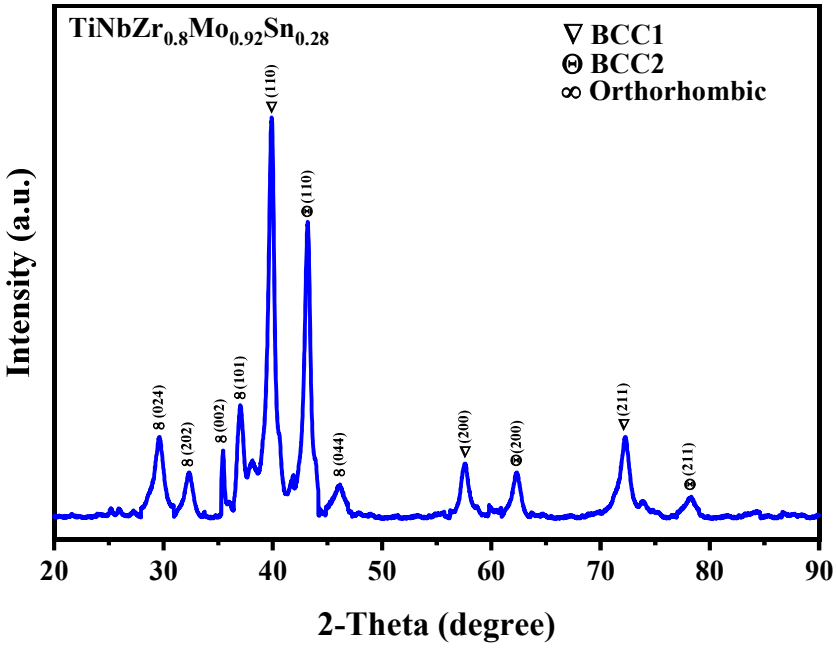

Fig. 4.11: XRD pattern of sintered $TiNbZr_{0.8}Mo_{0.92}Sn_{0.28}$ HEA

4.2 Microstructural analysis

4.2.1 Microstructural analysis of cpTi and Ti-6Al-4V

The microstructure plays an important role in defining the overall properties of an alloys. In load-bearing biomedical implants Ti and its alloys specially Ti-6Al-4V are

commercially recognized. Therefore, in the present study, the cpTi and Ti-6Al-4V are taken to compare the properties of the alloys. The microstructure of these cpTi and Ti-6Al-4V are shown in Fig. 4.12. The microstructure of cpTi shown in Fig. 4.12(a) reveals a single-phase α-Ti structure with an equiaxed grain morphology. This microstructure is characteristic of HCP crystal structures. While, the microstructure shown in Fig. 4.12(b) for Ti-6Al-4V exhibits a biphasic microstructure comprising primary α-phase and intergranular β-phase. The dark phase indicates the α-Ti phase and the bright phase indicates the β-Ti phase of the alloy.

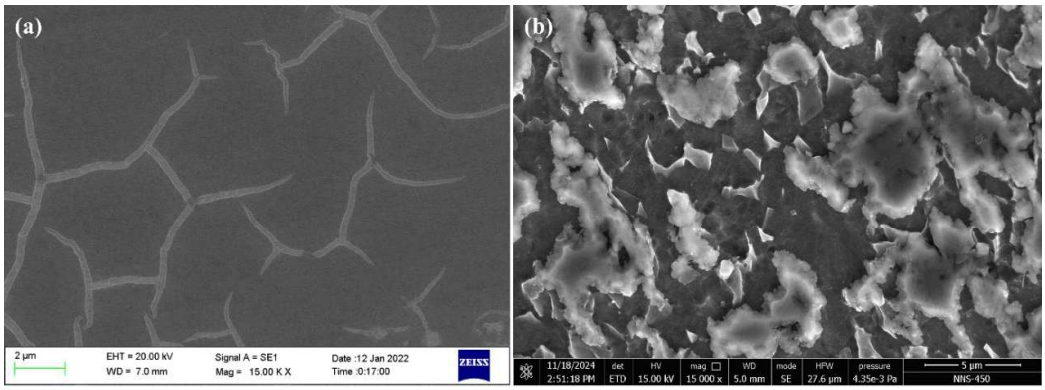

Fig. 4.12: SEM images of (a) cpTi and (b) Ti-6Al-4V

4.2.2 Microstructural analysis of sintered binary alloys

The microstructure of binary Ti-Nb and Ti-Zr alloys are shown in Fig. 4.13 and corresponding elemental mapping in Fig. 4.14. In Fig. 4.13(a), the microstructure of cpTi reveals a singular phase formation, devoid of any secondary phase. Conversely, the introduction of Nb into Ti results in the emergence of duplex phase, as evidenced by microstructural images depicted in Fig. 4.13(b-f). Within these images, the dark phase corresponds to α phase, whereas bright phase signifies the β phase within the alloys [191]. Addition of Nb in Ti resulted into formation of needle-like structure in all Ti-Nb alloys, also called dendrites. In contrast, there is no any needle like structure has been observed in cpTi microstructure. However, the dendrites formation starts with

incorporation of Nb, and it increases with Nb concentration in the alloys. In Ti-5Nb and Ti-10Nb, α phase with needle like dendritic microstructure is formed while increasing concentration of Nb results into smaller and wider dendrites with equiaxed β phase. There are less and needle like dendrites can be observed in Fig. 4.13(b) and Fig. 4.13(c), while a dense and maximum dendrites formation associated with equiaxed β grains can be seen in Fig. 4.13(f). Furthermore, the elemental mapping results presented in Fig. 4.14 confirm a uniform distribution of Nb across all the developed Ti-Nb alloys. With increasing Nb content, a higher Nb concentration is clearly visible in the β-phase regions. The dendritic microstructures observed in the alloys, particularly in Ti-15Nb, Ti-20Nb, and Ti-25Nb, are enriched with Nb, indicating the formation and stabilization of the β-phase due to Nb addition. Figure 4.15 displays the microstructural images of the sintered Ti-Zr alloys after etching with Kroll's reagent. It is observed that segregated equiaxial microstructure was obtained for the developed alloys that agreed with the previous studies [192]. The visual inspection of the microstructure is shown in Fig. 4.15. It reveals that two distinct phases have formed in alloys, as shown by the white and gray colours. However, it has been reported in the literature that despite having two different phase distributions, both have a hexagonal closed-packed structure and are classified as α-phase Ti alloys with different phase distributions; α-phase dominant with Ti and α-phase dominant with Zr [180,193]. The white colour indicates the α-phase dominant with Ti and the gray colour indicates the α-phase dominant with Zr. The reason for only obtaining the α-phase can be correlated with Zr's neutral behavior. When Zr is added to titanium, it stabilizes the α-phase upto 20% concentration [181]; as a result, increasing the Zr concentration increases the α-phase richer in Zr, which can be identified as the gray phase is increased in the Ti-20Zr sample. Here, also two phases are obtained with rich in Ti and rich in Zr α-phases. It was also found that as Zr content

increased, grains became coarser, and some fine pores and pits were discovered at grain boundaries, as previously documented in the literature [194,195]. The elemental mapping results presented in Fig. 4.16 reveal a uniform and homogeneous distribution of Zr across all the developed Ti-Zr alloy samples. The consistent dispersion of Zr suggests the successful formation of a solid solution without detectable phase segregation or clustering. This homogeneous elemental distribution further supports the compositional uniformity and the potential for improved mechanical and corrosion-resistant properties of the Ti-Zr alloys.

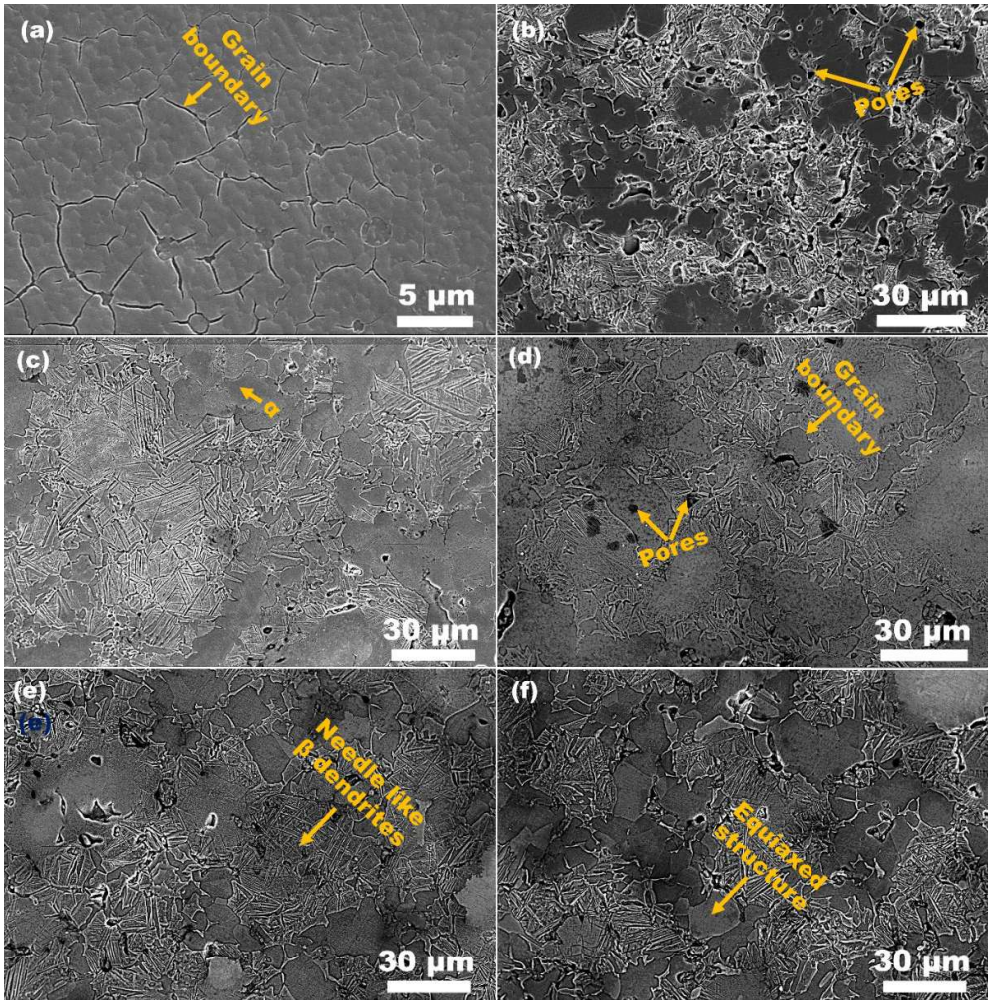

Fig. 4.13: SEM images of (a) cpTi, (b) Ti-5Nb, (c) Ti-10Nb, (d) Ti-15Nb, (e) Ti-20Nb, and (f) Ti-25Nb sintered alloys

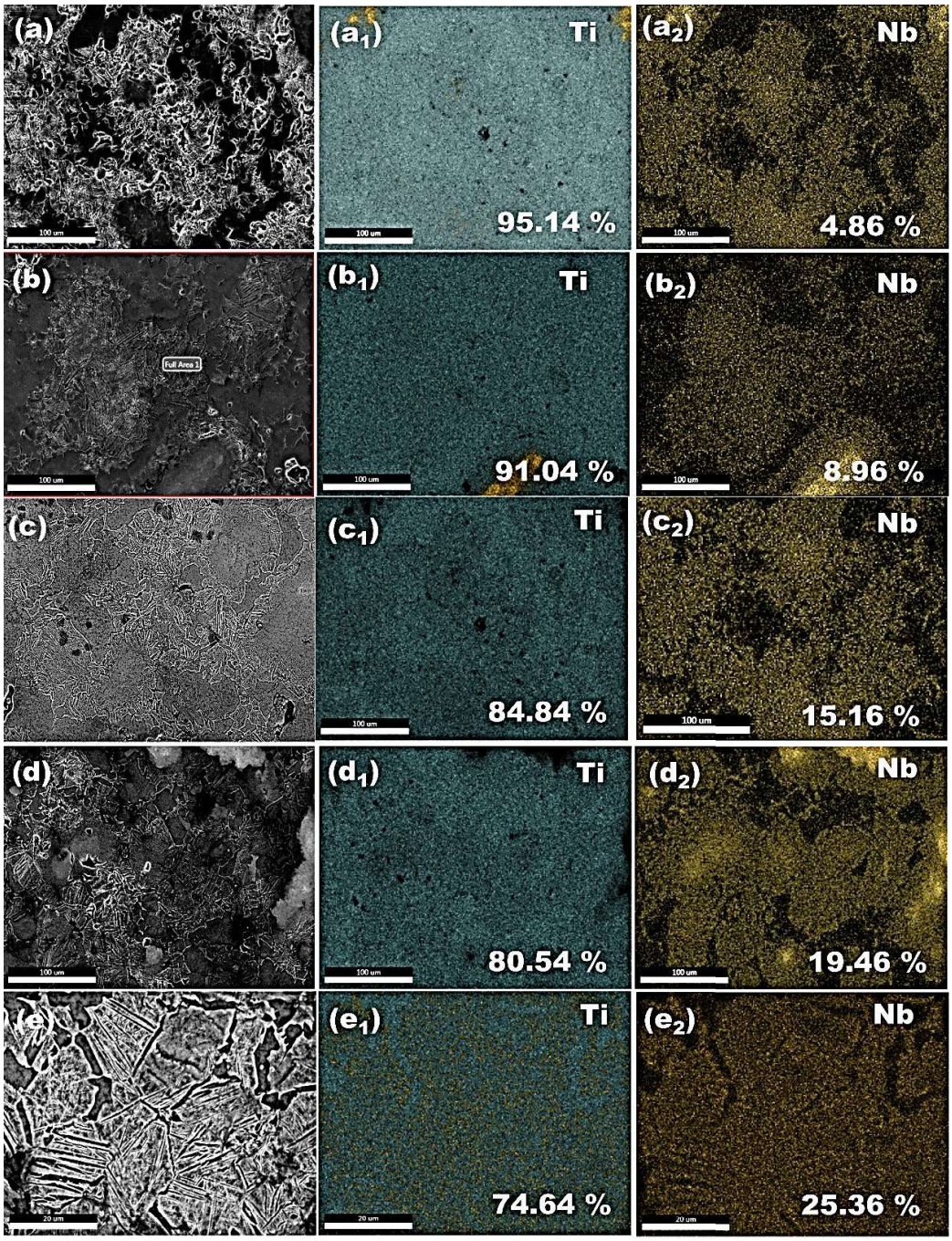

Fig. 4.14: Elemental mapping of (a) Ti-5Nb, (b) Ti-10Nb, (c) Ti-15Nb, (d) Ti-20Nb, and (e) Ti-25Nb sintered alloys

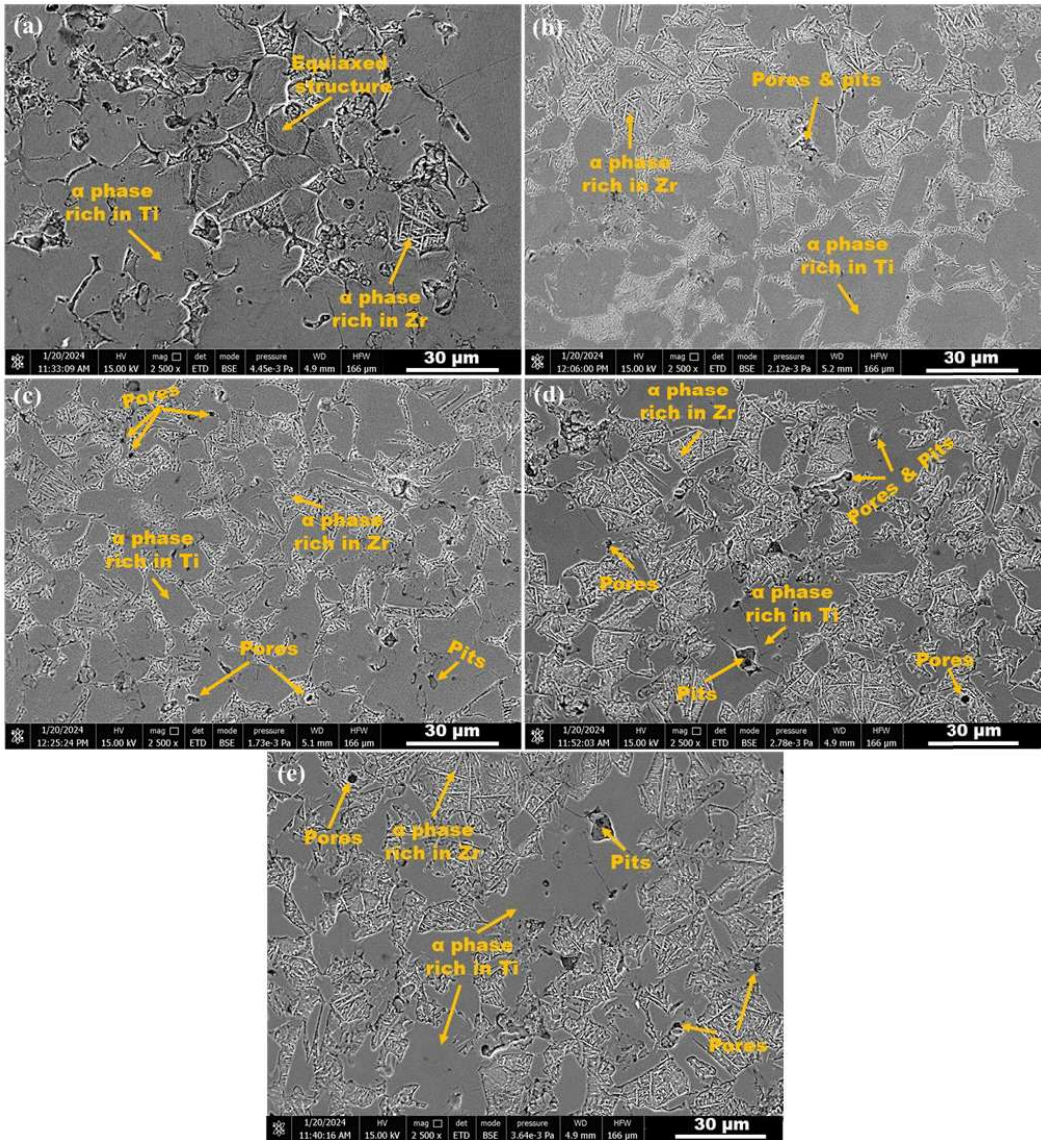

Fig. 4.15: SEM images of (a) Ti-5Zr, (b) Ti-10Zr, (c) Ti-15Zr, (d) Ti-20Zr, and (e) Ti-25Zr sintered alloys

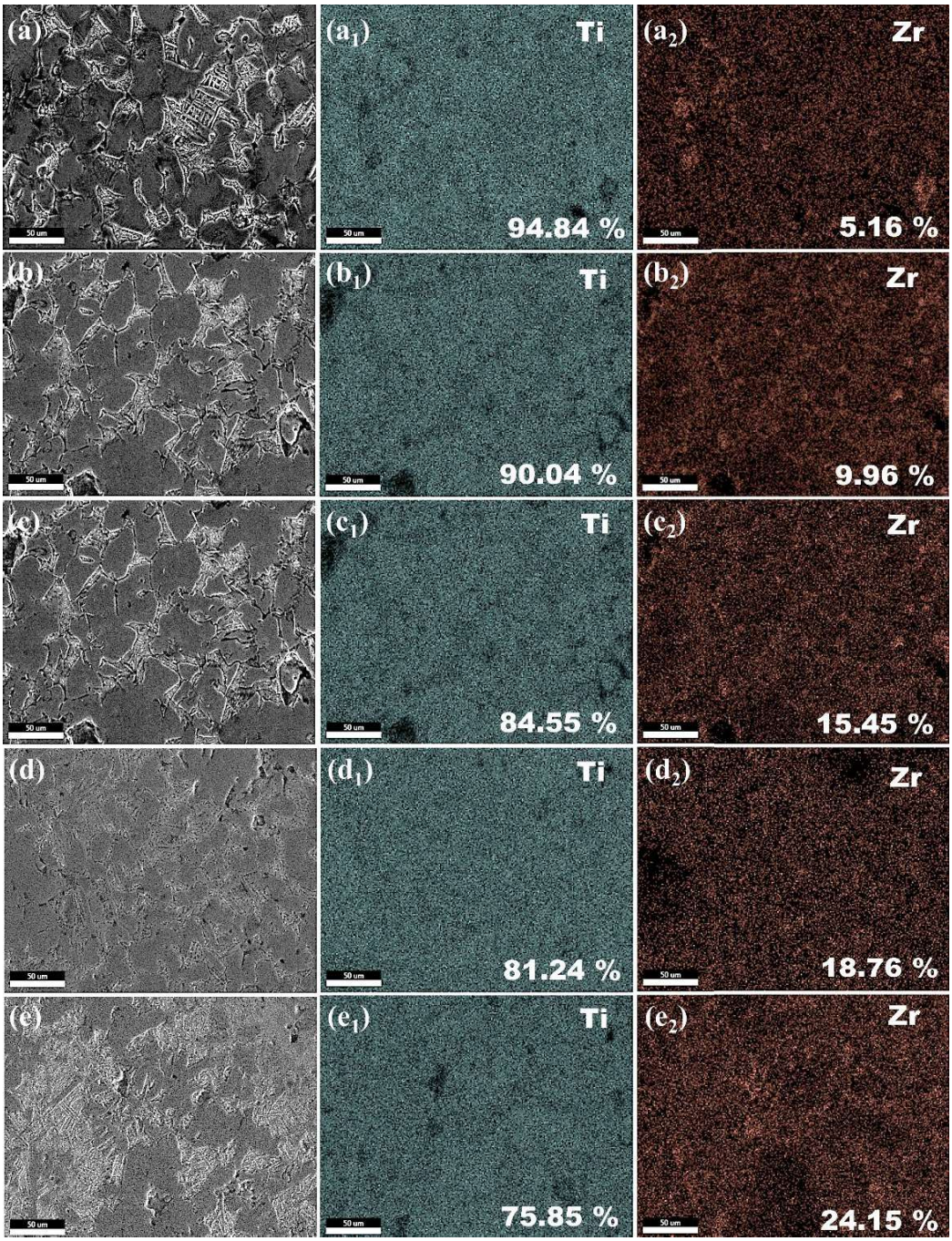

Fig. 4.16: Elemental mapping of (a) Ti-5Zr, (b) Ti-10Zr, (c) Ti-15Zr, (d) Ti-20Zr, and (e) Ti-25Zr sintered alloys

4.2.3 Microstructural analysis of sintered ternary alloys

The microstructure of etched samples of ternary Ti-10Zr-xNb alloys were taken through SEM and the images are shown in Fig. 4.17. Similar to binary Ti-xNb alloys, the Ti-10Zr-xNb alloys also have duplex microstructure which implies α-Ti with HCP and β-Ti with BCC structure. In the microstructural images shown in Fig. 4.17, porosities are higher as compared to the both binary alloys. The microstructure of this alloys is mainly attempted to increase the β-Ti phase and more porosity to achieve an optimum range of elastic modulus. It is reported in literature that the addition of Nb in the Ti-Zr alloy system suppress the β-Ti to α-Ti transformation during cooling and stabilize the β-Ti phase. The β-Ti phase having comparatively lower elastic modulus as compared to α-Ti phase. However, the elastic modulus of these alloys has still been reported higher in previous studies. In the present study, combined effect of Nb addition and incorporation of porosity to Ti-Zr alloy system is attempted to achieve the desired and optimum elastic modulus. The resulting effect of both are further discussed in the next sections. The elemental mapping of the sintered ternary Ti-10Zr-xNb alloys, as shown in Fig. 4.18, was conducted at lower magnification to cover a larger observation area for accurate compositional evaluation. The distribution maps reveal that both Zr and Nb are homogeneously dispersed within the Ti matrix, indicating the successful formation of a solid solution with no visible signs of phase segregation. This uniform elemental distribution across all compositions suggests effective interdiffusion during the sintering process. Furthermore, the presence of voids observed in the micrographs indicates the existence of porosity, which is characteristic of powder metallurgy-based fabrication routes.

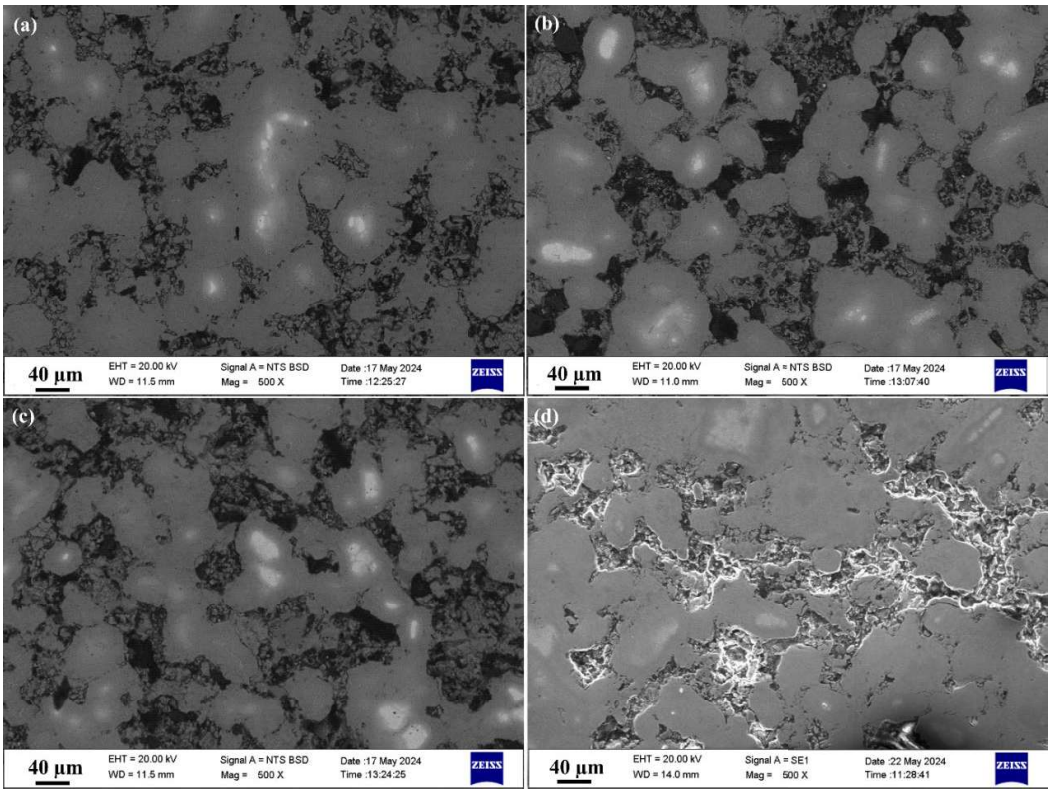

Fig. 4.17: SEM images of sintered ternary (a)Ti-10Zr-5Nb, (b) Ti-10Zr-10Nb, (c) Ti-10Zr-15Nb, (d) Ti-10Zr-20Nb alloys

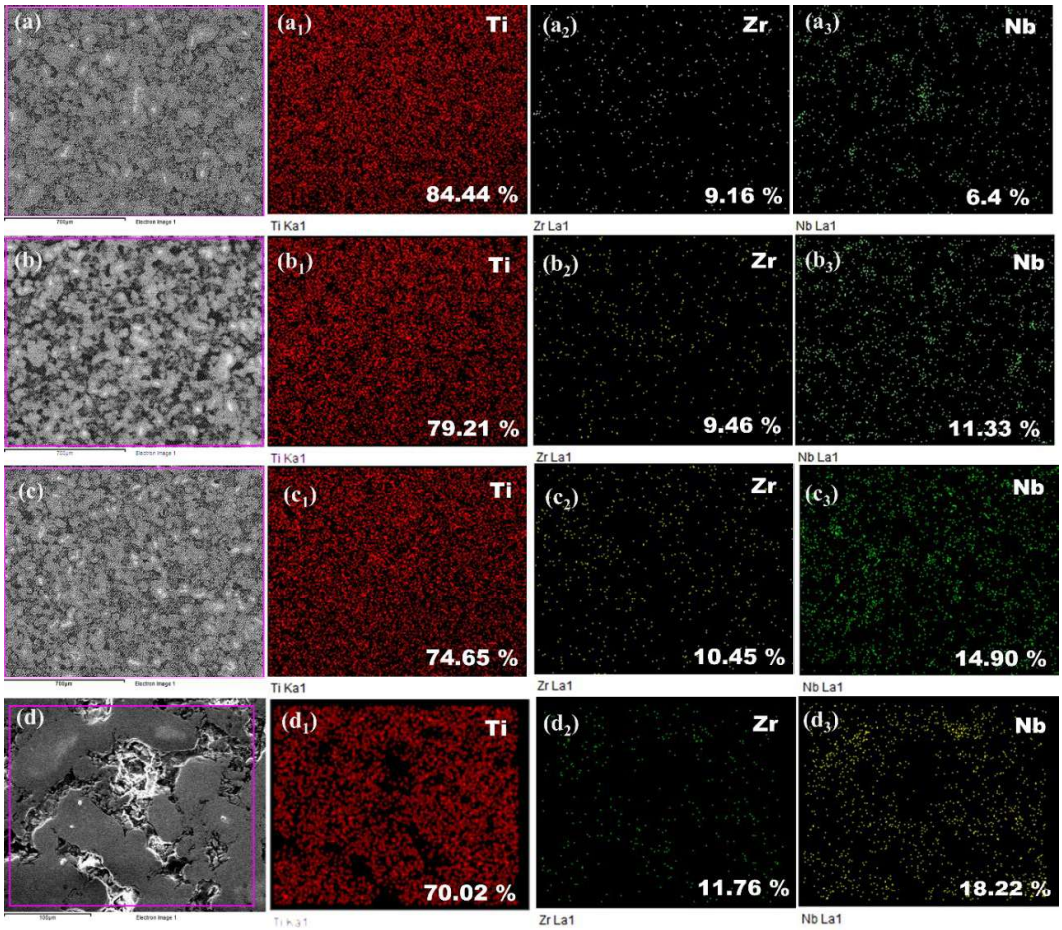

Fig. 4.18: Elemental mapping of sintered ternary (a)Ti-10Zr-5Nb, (b) Ti-10Zr-10Nb, (c) Ti-10Zr-15Nb, (d) Ti-10Zr-5Nb alloys

4.2.4 Microstructural analysis of sintered high entropy alloys

The high entropy alloys consist of five or more element and some of it diffuses during milling for longer duration. The microstructure of sintered alloys prepared from high energy ball milled alloyed powders is crucial for understanding the effect of microstructural effects on the properties such as mechanical, electrochemical, and tribological behaviour of the alloys. The images are shown in Fig. 4.19. The $TiNb_{1.5}Mo_{1.1}Zr_{1.15}Cu_{0.25}$ has three contrasts of color grey, white and black. Light elements tend to be concentrated in the dark contrast region, whereas heavy elements exhibit a centralized distribution in the light contrast region [196]. The gray color enriched with Ti and Nb corresponds to BCC1 phase. White color enriched with Zr

correspond to orthorhombic phase and black color enriched with Cu, Ti which shows tetragonal phase. The SEM results are confirmed by the XRD analysis. In the XRD results, the BCC1 phase shows the highest intensity, indicating it as the major phase. This is consistent with the SEM images, where the BCC1 phase is the most prominent. Additionally, the XRD data shows that the orthorhombic phase has the least intensity, while the tetragonal phase has a higher intensity than the orthorhombic phase. In the SEM images, the black color corresponding to the tetragonal phase is more prevalent than the white color representing the orthorhombic phase. When niobium (Nb) is added to a titanium alloy, it serves as β stabilizer, enhancing the alloy's preservation and contributing to the desirable properties of the resulting high-entropy alloy (HEA).

The $TiNbZr_{0.8}Mo_{0.92}Sn_{0.28}$ also has three contrasts of color light grey, gray and black. The gray color enriched with Ti and Nb corresponds to BCC1 phase. Light gray color enriched with Zr corresponds to orthorhombic phase and black color enriched with Mo which shows BCC2 phase. As previous the SEM results are confirmed by the XRD analysis. Further it can be seen that dual or multiphase alloys are renowned for their impressive mechanical strength, excellent fracture toughness, and enhanced resistance to corrosion [197].

The elemental mapping image for $TiNb_{1.5}Mo_{1.1}Zr_{1.15}Cu_{0.25}$ are shown Fig. 4.20(a) with corresponding elemental distribution in Fig. 4.20(a_1-a_5). The result shows the presence of Ti, Nb, Zr, Mo, and Cu on the sintered alloys and are distributed throughout the whole areas, indicating a homogenous solid solution of these elements. Moreover, elemental mapping image for $TiNbZr_{0.8}Mo_{0.92}Sn_{0.28}$ is shown in Fig. 4.20(b) with corresponding elemental distribution in Fig. 4.20(b_1-b_5). The result shows similar with elemental composition different from $TiNb_{1.5}Mo_{1.1}Zr_{1.15}Cu_{0.25}$. The elements are also evenly distributed in this alloy indicating homogenous and stable solid solution.

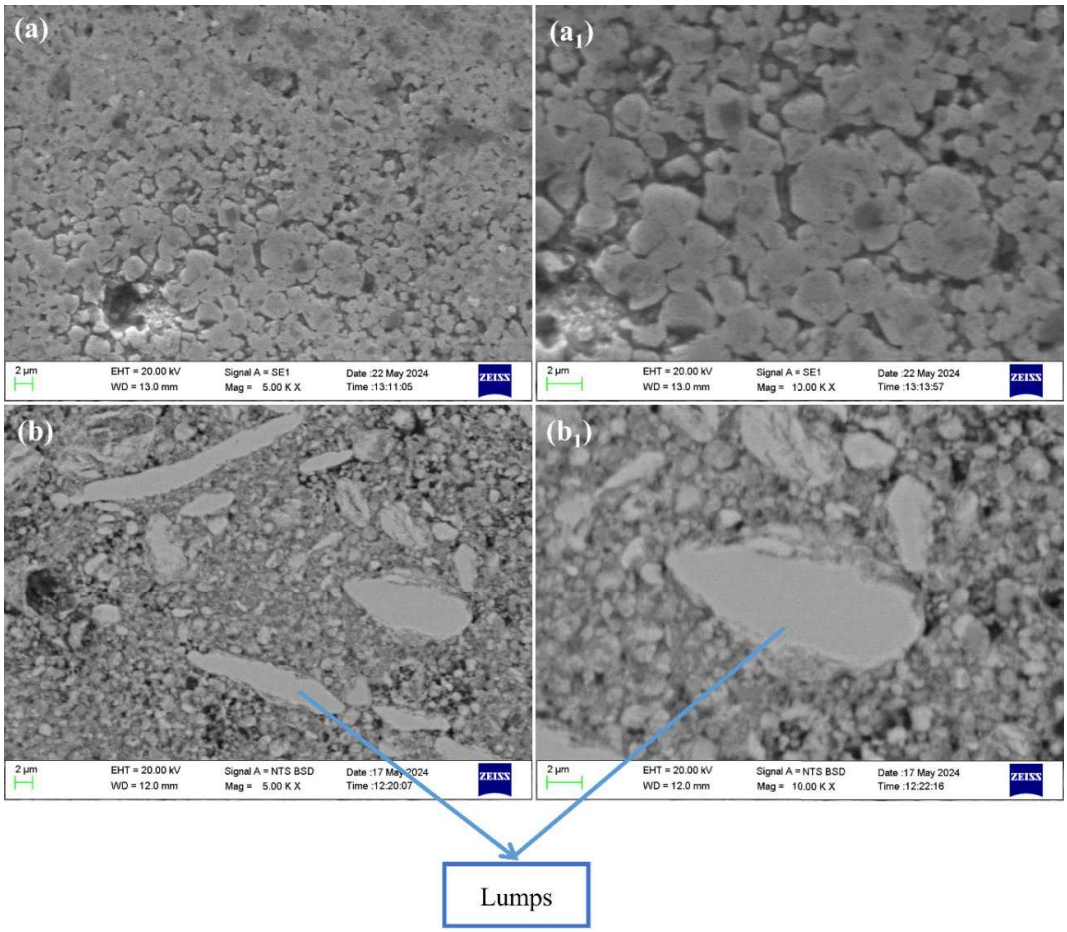

Fig. 4.19: SEM images of (a) sintered $TiNb_{1.5}Mo_{1.1}Zr_{1.15}Cu_{0.25}$ at 5000x, (b) sintered $TiNb_{1.5}Mo_{1.1}Zr_{1.15}Cu_{0.25}$ at 10000x, (c) sintered $TiNbZr_{0.8}Mo_{0.92}Sn_{0.28}$ at 5000x, (d) sintered $TiNbZr_{0.8}Mo_{0.92}Sn_{0.28}$ at 10000x

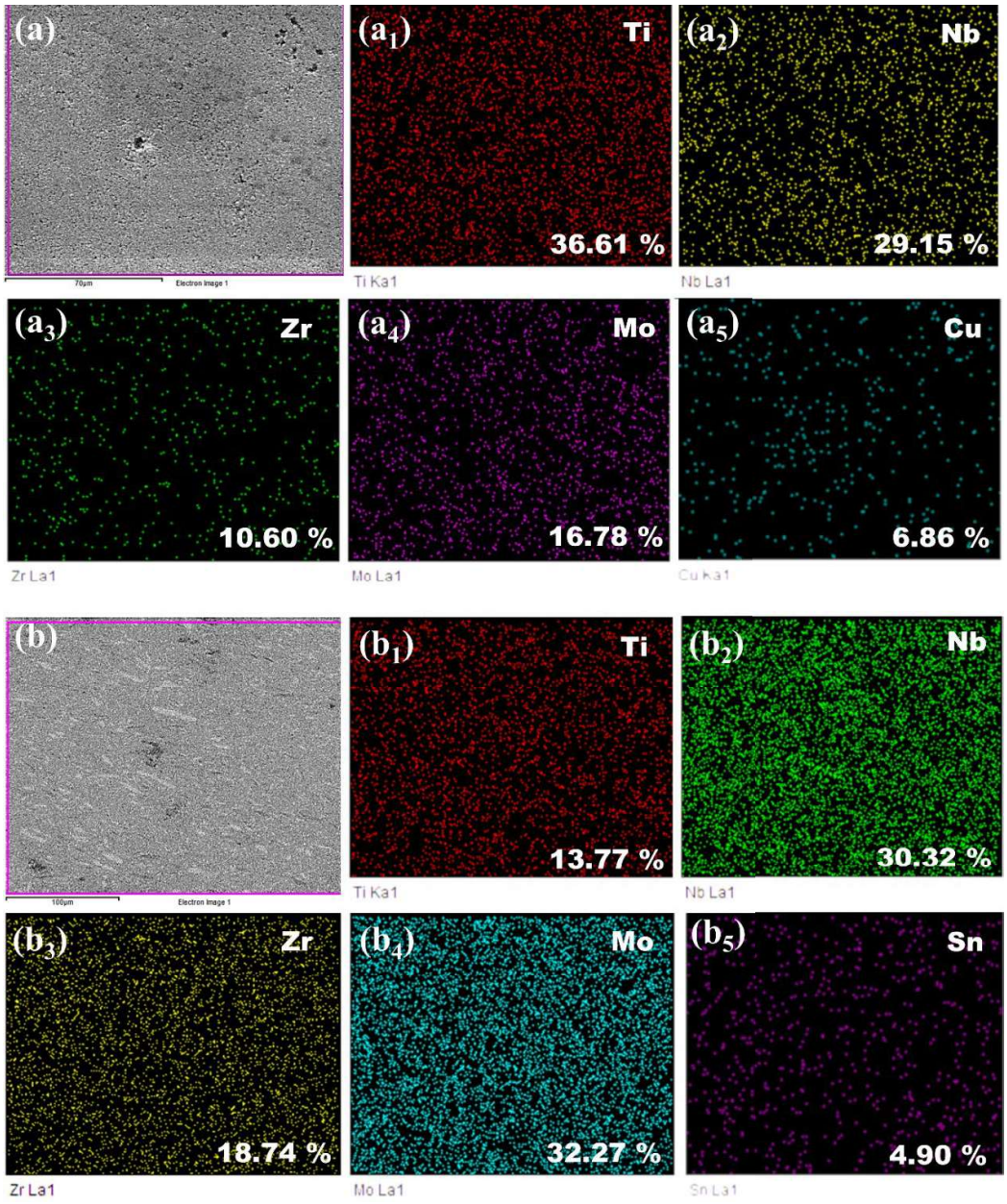

Fig. 4.20: Elemental mapping image of (a) sintered $TiNb_{1.5}Mo_{1.1}Zr_{1.15}Cu_{0.25}$ and (a_1-a_5) corresponding elemental distribution (b) sintered $TiNb_{1.5}Mo_{1.1}Zr_{1.15}Cu_{0.25}$ and (b_1-b_5) corresponding elemental distribution

4.3 Density and porosity

4.3.1 Density and porosity of cpTi and Ti-6Al-4V

The density of cpTi and Ti-6Al-4V were determined to compare with the developed alloys. Table 4.1 shows the theoretical and sintered density of cpTi and Ti-6Al-4V along with the porosity calculated from the formula.

Table 4.1: Theoretical and actual density of cpTi and Ti-6Al-4V alloy

Sample composition	Sintered density (g/cm^3)	Theoretical density (g/cm^3)	Porosity (In percent)
cpTi	–	4.506	–
Ti-6Al-4V	–	4.429	–

4.3.2 Density and porosity of sintered binary alloys

The density of materials has a critical influence on overall performance and suitability of biomedical implants. In dental implants, joint replacements, and bone fixation devices, lightweight implants are preferred, which reduces the burden on patients. Ti alloys provide adequate strength while possessing lower density in contrast to other metallic implants such as Co-Cr alloys and stainless steel, making them advantageous for load-bearing applications. The densities and porosities obtained by Archimedes principle for binary Ti-Nb and Ti-Zr alloys are given in Table 4.2 and Table 4.3. Table 4.2 presents the theoretical and experimental density values for Ti-Nb alloys. It is observed that both theoretical and sintered densities of Ti-Nb alloys increases with increasing the concentration of Nb. With the help of theoretical and experimental densities the porosity percentage are calculated as shown in Table 4.2. The porosity percentage are increasing slightly with addition of Nb where the maximum porosity of 15.0577 ± 0.579 is observed for Ti-25Nb alloy. Table 4.3 displays the theoretical density, sintered density, and porosity of sintered Ti-Zr alloys. It is observed that the

theoretical as well sintered density of the alloys increases with increasing zirconium contents. This can be related to the fact that density of zirconium is higher than titanium which leads to an increment in density of alloys with the inclusion of Zr [198], which can also be seen in theoretical density. However, no significant difference is observed in the porosity of alloys. This may be because the same compaction pressure and sintering temperature have been used to develop the alloys.

Table 4.2: Theoretical densities, sintered density, and percentage porosity of Ti-Nb alloys

Sample composition	Sintered density (g/cm^3)	Theoretical density (g/cm^3)	Porosity (In percent)
Ti-5Nb	4.0965 ± 0.012	4.6196	11.3234 ± 0.268
Ti-10Nb	4.1410 ± 0.008	4.7343	12.5327 ± 0.156
Ti-15Nb	4.2105 ± 0.017	4.8551	13.2768 ± 0.356
Ti-20Nb	4.2374 ± 0.027	4.9821	14.9468 ± 0.534
Ti-25Nb	4.3457 ± 0.030	5.1161	15.0577 ± 0.579

Table 4.3: Theoretical density, sintered density and percentage porosity of sintered Ti-Zr alloys

Sample composition	Theoretical density (g/cm^3)	Sintered density (g/cm^3)	Porosity (In percent)
Ti-5Zr	4.609	4.2009 ± 0.0162	8.85 ± 0.35
Ti-10Zr	4.6806	4.2592 ± 0.0126	9.00 ± 0.27
Ti-15Zr	4.754	4.3291 ± 0.0081	8.93 ± 0.17
Ti-20Zr	4.8302	4.3908 ± 0.0087	9.09 ± 0.18
Ti-25Zr	4.8853	4.4489 ± 0.0032	8.93 ± 0.16

4.3.3 Density and porosity of sintered ternary alloys

Similar to binary alloys, the densities and porosities obtained for ternary Ti-10Zr-xNb alloys are given in Table 4.4. This table presents the sintered density, theoretical density, and porosity of Ti-10Zr-xNb alloys with varying niobium (Nb) content (5-20 wt.%). The sintered density increases progressively from 3.476 g/cm^3 to 3.866 g/cm^3 with rising Nb content, reflecting the improved densification with higher Nb addition. Similarly, the theoretical density also increases (4.769 g/cm^3 to 5.157 g/cm^3), as Nb has a higher atomic mass compared to titanium and zirconium. Despite the increase in density, porosity decreases slightly with rising Nb content, from 27.13% to 25.04%, indicating better particle packing and reduced voids during sintering. This trend suggests that higher Nb content enhances sintering efficiency, leading to improved material consolidation and potentially better mechanical properties, crucial for biomedical applications.

Table 4.4: Theoretical density, sintered density and percentage porosity of Ti-10Zr-xNb alloys

Sample	Sintered density (g/cm^3)	Theoretical density (g/cm^3)	Porosity (In Percent)
Ti-10Zr-5Nb	3.476	4.769	27.13
Ti-10Zr-10Nb	3.571	4.892	27.00
Ti-10Zr-15Nb	3.682	5.021	26.68
Ti-10Zr-20Nb	3.866	5.157	25.04

4.3.4 Density and porosity of sintered high entropy alloys

The densities and porosities of sintered high entropy alloys are given in Table 4.5. It can also be seen that the theoretical and actual density values of $TiNb_{1.5}Mo_{1.1}Zr_{1.15}Cu_{0.25}$ and $TiNbZr_{0.8}Mo_{0.92}Sn_{0.28}$ are almost the same because it

shares four similar elements with nearly identical compositions and preparation of both samples follows same procedure.

The porosity of $TiNbZr_{0.8}Mo_{0.92}Sn_{0.28}$ is 14.59% and that of $TiNb_{1.5}Mo_{1.1}Zr_{1.15}Cu_{0.25}$ is 9.27%. The higher value of porosity makes $TiNbZr_{0.8}Mo_{0.92}Sn_{0.28}$ more promising material for biomedical implants.

Table 4.5: Theoretical density, sintered density and percentage porosity of sintered HEAs

Sample	Sintered density (g/cc)	Theoretical density (g/cc)	Porosity (In Percent)
$TiNb_{1.5}Mo_{1.1}Zr_{1.15}Cu_{0.25}$	6.630	7.308	9.27
$TiNbZr_{0.8}Mo_{0.92}Sn_{0.28}$	6.410	7.505	14.59

4.4 Mechanical properties

4.4.1 Hardness

4.4.1.1 Hardness of cpTi and Ti-6Al-4V

The hardness was measured for cpTi and Ti-6Al-4V to compare it with different developed alloys. The hardness values are plotted in form of bar graph and shown in Fig. 4.21. The cpTi which comprises a single α phase have lower hardness of about 178 HV, while Ti-6Al-4V consist of duplex α + β phase have higher hardness of 350 HV. The higher hardness of Ti-6Al-4V is mainly obtained due to its alloying with Al and V. Al is a α phase stabilizer while V is β-phase stabilizer. These stabilizers strengthen the α-phase and introduce the stable β-phase of titanium with duplex microstructure results into increased hardness of Ti-6Al-4V.

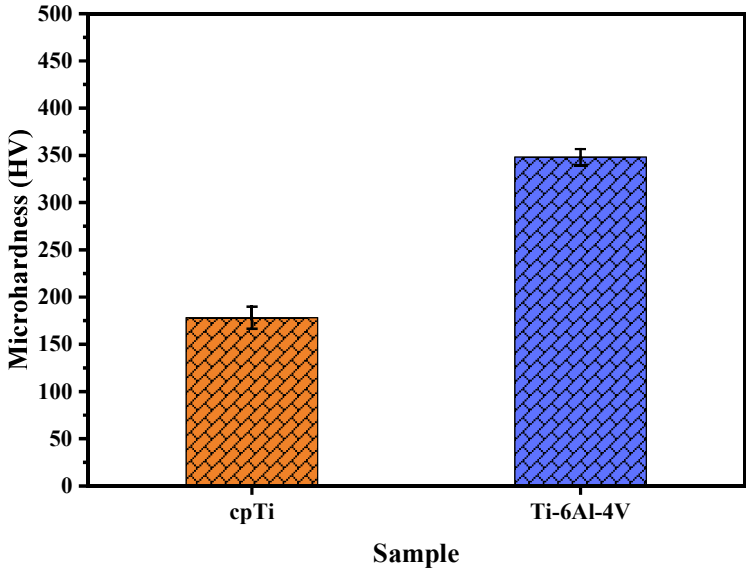

Fig. 4.21: Vickers hardness of cpTi and Ti-6Al-4V alloy

4.4.1.2 Hardness of sintered binary alloys

The microhardness obtained from Vickers hardness test for both Ti-Nb and Ti-Zr binary alloys are shown in Fig. 4.22 and Fig. 4.23. The microhardness values obtained from Vickers hardness tests for various Ti-Nb alloys are depicted in Fig. 4.22. For cpTi, the hardness value was 178.08 ± 11.63 HV, whereas for the Ti-Nb alloys, it ranges from 301.23 ± 17.21 to 403.23 ± 21.38 HV. The Ti-10Nb alloy exhibits the highest hardness, while cpTi shows the lowest. Comparatively, Ti-5Nb and Ti-10Nb demonstrate higher hardness value than other Ti-Nb alloys. Incorporation of Nb up to 10 wt.% enhances the hardness of Ti-10Nb up to 403.23 ± 21.38 HV, surpassing cpTi. Further Nb additions beyond 10 wt.% leads to decrease in hardness upto 359.35 ± 19.73, 291.92 ± 22.52 HV for Ti-15Nb and Ti-20Nb alloys respectively. Moreover, the hardness value again increased up to 396.81 ± 12.94 HV in Ti-25Nb alloy. The increase in hardness of Ti-5Nb and Ti-10Nb alloys is attributed to solid solution strengthening from Nb addition. Adding up to 10% Nb results in the formation of needle-like β dendrites along with the α-phase. Further Nb additions beyond 10 wt.% lead to the formation of wider dendrites and equiaxed β grains, accompanied by the α-phase. This results in a decrease

in hardness due to the increased dominance of the β-phase in the alloys. The β-phase typically exhibits lower hardness compared to the α-phase, leading to an overall reduction in the hardness of the Ti alloys with higher Nb concentration [199]. Consequently, the hardness of Ti-15Nb and Ti-20Nb alloys decreases due to the presence of a larger β-phase. Moreover, the unexpected increase in hardness in Ti-25Nb is consistent with previous studies and is attributed to the presence of a minor quantity of the ω phase at Nb concentrations between 20% and 27.5%. The ω phase has a primitive hexagonal structure similar to the α-phase and is typically difficult to detect due to instrumental limitations [200,201]. Figure 4.23 shows the Vickers hardness of produced Ti-Zr alloys. The developed alloys have hardness values of 477.59 ± 30.216, 539.05 ± 27.091, 528.78 ± 23.65 and 488.97 ± 39.732 HV, respectively. These values are much greater than the hardness of commercially pure titanium (200.26 HV) and Ti-6Al-4V (340.51 HV), which are often used in biomedical implant materials [202]. The maximum hardness was observed for Ti-10Zr alloy (539.05 ± 27.091 HV), and it has been observed that adding up to 10 wt.% zirconium to alloys causes them to become harder. Thus, solid solution strengthening the α phase is primarily responsible for the increase in hardness [203]. Above 10 wt.%, increasing Zr concentration results in a slight decrease in hardness (528.78 ± 23.65 HV and 488.97 ± 39.732 for Ti-15Zr and Ti-20Zr respectively). Similar outcomes have been documented in the literature and are attributed to the fact that Ti-10Zr alloy contains a higher amount of oxygen in the solid solution as compared to Ti-15Zr and Ti-20Zr alloys [204].

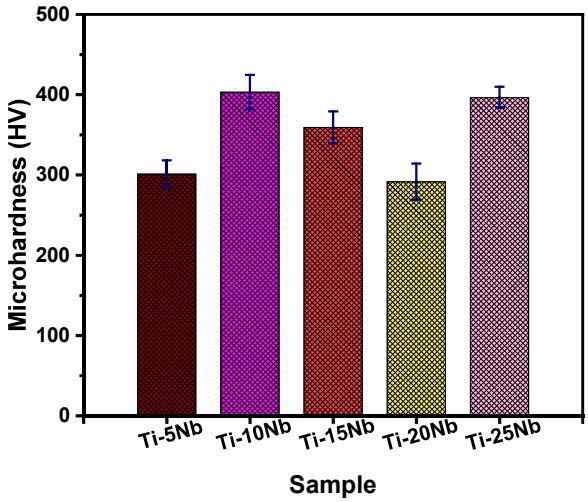

Fig. 4.22: Vickers hardness of sintered Ti-xNb alloys

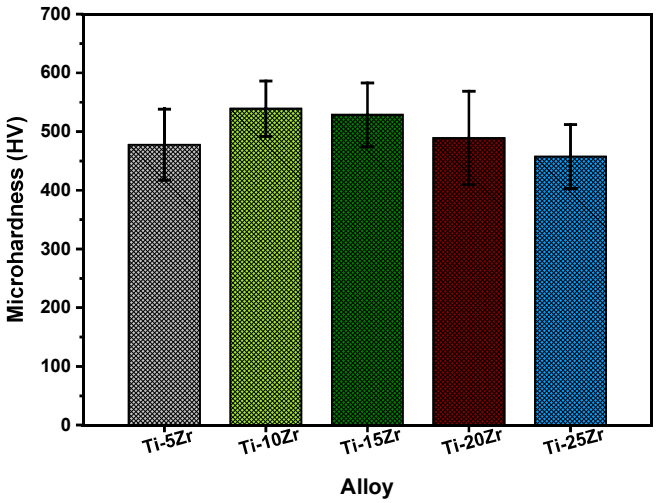

Fig. 4.23: Vickers hardness of sintered Ti-xZr alloys

4.4.1.3 Hardness of sintered ternary alloys

The hardness graph shown in Fig. 4.24 for Ti-10Zr-xNb alloys shows the variation in hardness with increasing niobium (Nb) content (5, 10, 15, and 20 wt.%). The Ti-10Zr-5Nb alloy exhibits the highest hardness, followed closely by Ti-10Zr-10Nb, both maintaining values around 380 and 340 HV. A significant drop in hardness is observed for Ti-10Zr-15Nb, which shows the lowest value, indicating a weakening effect likely due to microstructural changes or reduced phase strengthening. However, the Ti-10Zr-20Nb alloy demonstrates an improvement in hardness compared to 15Nb, suggesting the re-establishment of strengthening mechanisms, such as beta-phase stabilization and

solid solution strengthening by niobium [205].

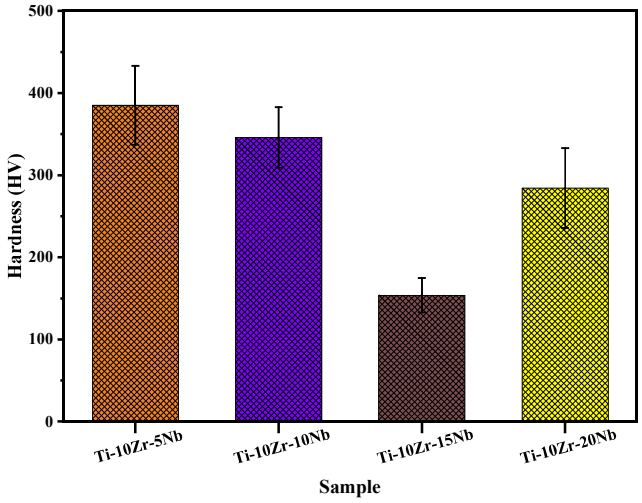

Fig. 4.24: Vickers hardness of sintered Ti-10Zr-xNb alloys

4.4.1.4 Hardness of sintered high entropy alloys

The Vickers hardnesses of sintered high entropy alloys are shown in Fig. 4.25. The average Vickers hardness number (HV) for $TiNb_{1.5}Mo_{1.1}Zr_{1.15}Cu_{0.25}$ is 470.1 ± 21.5 HV and for $TiNbZr_{0.8}Mo_{0.92}Sn_{0.28}$ is 481 ± 37.9 HV. One of the main reasons for the high hardness value of both HEAs might be the incorporation of Mo, because Mo can play a positive role in improvement of hardness of alloy material [206]. Additionally, the developed HEAs have a BCC structure, and it can be seen that BCC phase alloys show high hardness values [207].

Although the amount of Mo in $TiNb_{1.5}Mo_{1.1}Zr_{1.15}Cu_{0.25}$ is more than in $TiNbZr_{0.8}Mo_{0.92}Sn_{0.28}$ still hardness of $TiNbZr_{0.8}Mo_{0.92}Sn_{0.28}$ is greater than that of $TiNb_{1.5}Mo_{1.1}Zr_{1.15}Cu_{0.25}$. The observed enhancement in hardness can be attributed to the solid solution strengthening effect of Sn. Tin atoms (atomic radius~1.58 Å), being larger than Ti (atomic radius~1.47 Å), distort the lattice and hinder dislocation motion, thereby increasing the material's hardness. Additionally, previous studies have reported that Sn can contribute to microstructural refinement, which may further enhance

mechanical properties [150]. Hindering dislocations from moving freely making plastic deformation more challenging that's why hardness of Sn added HEA is more. Upon comparing the hardness values with those of cpTi (200.26 HV) and Ti-6Al-4V (340.51 HV), commonly used for bio implant materials, it can be observed that both HEAs exhibit significantly higher hardness values.

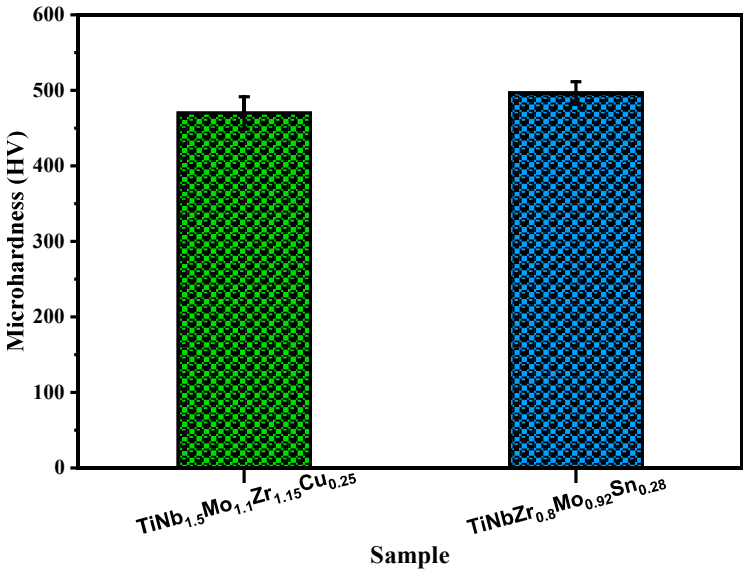

Fig. 4.25: Vickers hardness of sintered $TiNb_{1.5}Mo_{1.1}Zr_{1.15}Cu_{0.25}$ and $TiNbZr_{0.8}Mo_{0.92}Sn_{0.28}$ high entropy alloys

4.4.2 Elastic modulus

4.4.2.1 Elastic modulus of cpTi and Ti-6Al-4V

The load displacement curves obtained from the micro indentation test for cpTi and Ti-6Al-4V is shown in Fig. 4.26. It is observed that the displacement for cpTi is more than Ti-6Al-4V at the same indentation load, which indicates that the elastic modulus of Ti-6Al-4V is higher as compare to the cpTi. The elastic modulus obtained from the Oliver-Pharr method is given in Table 4.6. The elastic modulus obtained for cpTi is 117.53 ± 8.13 GPa, while the elastic modulus of Ti-6Al-4V is 125 ± 4.35.

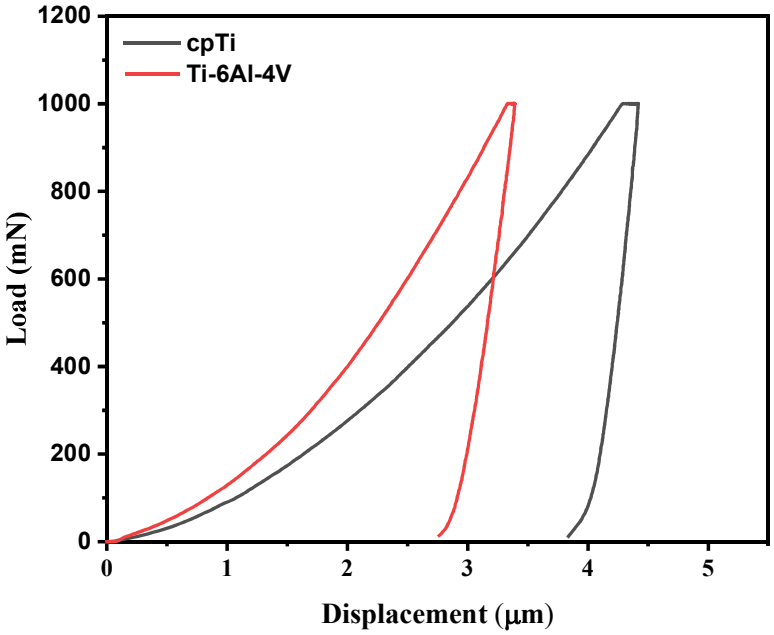

Fig. 4.26: Load displacement curve obtained for cpTi and Ti-6Al-4V from microindentation testing

Table 4.6: Elastic modulus of cpTi and Ti-6Al-4V alloy

Sample	cpTi	Ti-6Al-4V
Elastic modulus (GPa)	117.53 ± 8.13	125 ± 4.35

4.4.2.2 Elastic modulus of sintered binary alloys

The load displacement curve obtained from the microindentation testing for binary Ti-xNb and Ti-xZr alloys are presented in Fig. 4.27. The corresponding values of elastic modulus obtained from Oliver and Pharr method is given in Table 4.7. Nb incorporation and the fabrication of these Ti-Nb alloys via the PM route resulted in decreased elastic modulus across all alloys. Ti-20Nb exhibited the lowest elastic modulus of 43.47 ± 4.9 GPa, while Ti-10Nb alloy displayed highest of 54.65 ± 6.49 GPa. Moreover, these values are far lower than cpTi having elastic modulus of 117.53 ± 8.13 GPa. The microstructure and phase composition of these alloys also have a significant impact on

their mechanical characteristics [184]. The microstructure of Ti-5Nb and Ti-10Nb alloys exhibits a typical dendritic structure, which impedes dislocation movement and thus strengthens these alloys [208]. Moreover, when Nb addition exceeds 10 wt.%, the typical dendritic structure evolves into a microstructure with both dendritic and equiaxed β-phases. Due to increased proportion of the β-phase, decreased percentage of the α phase, and the weaker lattice bond strength of the β-phase crystals [89,209], this type of microstructure is less resistant to dislocation movement compared to the typical dendrites. Hence, this leads to a reduction in elastic modulus in Ti-15Nb and Ti-20Nb alloys [210]. Although, the increase in elastic modulus in Ti-25Nb is mainly observed due to its additional ω phase.

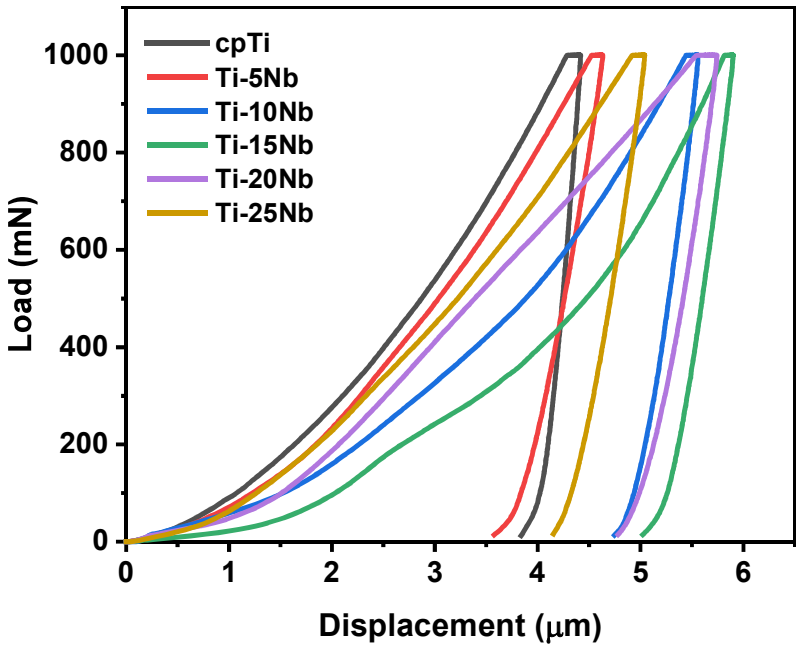

Fig. 4.27: Load displacement curve obtained for cpTi and binary Ti-xNb alloys from microindentation testing

Table 4.7: Elastic modulus of sintered Ti-xNb alloys

Sample	Ti-5Nb	Ti-10Nb	Ti-15Nb	Ti-20Nb	Ti-25Nb
Elastic modulus (GPa)	50.87 ± 5.81	54.65 ± 6.49	46.42 ± 6.52	43.47 ± 4.9	50.91 ± 3.33

Figure 4.28 shows the load displacement curve of Ti-xZr alloys and their elastic modulus values are presented in Table 4.8. The elastic modulus values of sintered Ti-xZr alloys exhibit variations with increasing Zr content. The initial addition of Zr (Ti-5Zr and Ti-10Zr) increases the modulus, likely due to the solid solution strengthening effect and improved atomic bonding within the alloy matrix. However, further increments (Ti-15Zr and Ti-20Zr) result in a slight decrease, which may be attributed to lattice distortion and the introduction of stress concentrations that compromise stiffness. The significant reduction observed for Ti-25Zr (71.46 GPa) could be due to the formation of a softer secondary phase or microstructural changes like increased porosity or grain boundary weakening. These variations highlight the complex interplay of alloy composition and microstructure on mechanical properties, essential for tailoring biomedical implants.

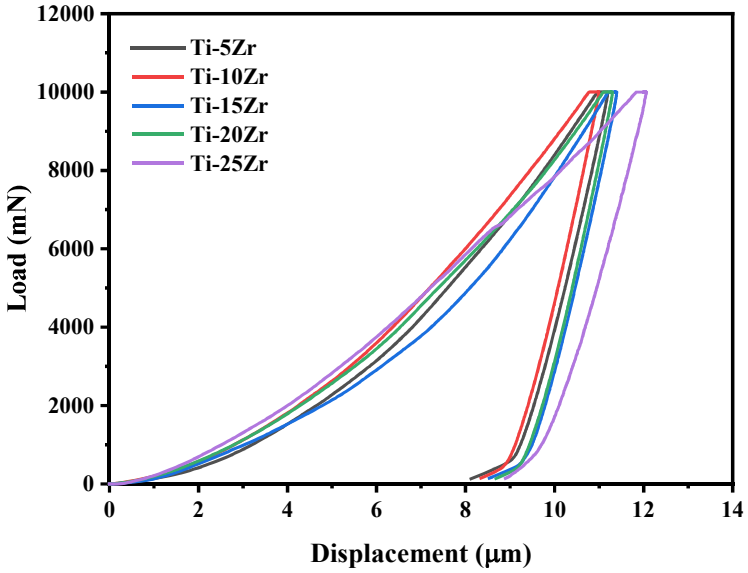

Fig. 4.28: Load displacement curve for binary Ti-xZr alloys from microindentation testing

Table 4.8: Elastic modulus of sintered Ti-xZr alloys

Sample	Ti-5Zr	Ti-10Zr	Ti-15Zr	Ti-20Zr	Ti-25Zr
Elastic modulus (GPa)	87.54	94.08	87.30	91.13	71.46

4.4.2.3 Elastic modulus of sintered ternary alloys

Figure 4.29 shows the load displacement curve for Ti-10Zr-xNb and the corresponding elastic modulus are given in Table 4.9. The elastic modulus of sintered Ti-10Zr-xNb alloys demonstrates a decreasing trend with increasing Nb content, except for Ti-10Zr-15Nb, which shows a slight increase. The reduction in elastic modulus is attributed to the β-phase stabilizing effect of Nb, which promotes the formation of a β-Ti phase with a lower modulus compared to α-Ti. This characteristic aligns these alloys with the modulus of human bone (~10-30 GPa), thereby minimizing stress shielding effects in biomedical implants. The slight anomaly at 15Nb may be due to microstructural

variations or partial α-phase retention. Overall, the alloys exhibit elastic moduli suitable for load-bearing implant applications.

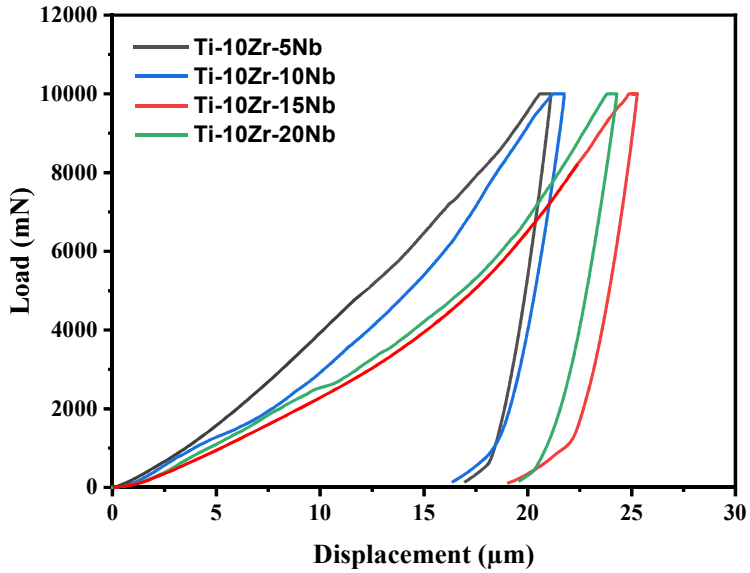

Fig. 4.29: Load displacement curve obtained for ternary Ti-10Zr-xNb alloys from microindentation testing

Table 4.9: Elastic modulus of sintered Ti-10Zr-xNb alloys

Sample	Ti-10Zr-5Nb	Ti-10Zr-10Nb	Ti-10Zr-15Nb	Ti-10Zr-20Nb
Elastic modulus (GPa)	41.51	35.23	30.43	32.51

4.4.2.4 Elastic modulus of sintered high entropy alloys

Figure 4.30 shows the load displacement plot for both the high entropy alloys and their corresponding elastic modulus are given in Table 4.10. The elastic modulus of $TiNb_{1.5}Mo_{1.1}Zr_{1.15}Cu_{0.25}$ and $TiNbZr_{0.8}Mo_{0.92}Sn_{0.28}$ high-entropy alloys (HEAs) are 69.12 GPa and 64.56 GPa, respectively. These results indicate that $TiNbZr_{0.8}Mo_{0.92}Sn_{0.28}$ exhibits a lower elastic modulus compared to $TiNb_{1.5}Mo_{1.1}Zr_{1.15}Cu_{0.25}$. The porosity of $TiNbZr_{0.8}Mo_{0.92}Sn_{0.28}$ is 14.59% and that of

$TiNb_{1.5}Mo_{1.1}Zr_{1.15}Cu_{0.25}$ is 9.27%. Due to high porosity the effective load-bearing area, reduces which make the material less stiff. The voids disrupt the uniform transfer of stress and act as stress concentrators, leading to earlier and more localized deformation. As a result, the material exhibits reduced resistance to elastic deformation. hence reduced young's modulus. Previous results are evident that the elastic modulus decreases with porosity [211]. The reduced modulus of $TiNbZr_{0.8}Mo_{0.92}Sn_{0.28}$ suggests better compatibility with the elastic properties of human bone (10-30 GPa), potentially minimizing stress shielding effects when used as a load-bearing implant.

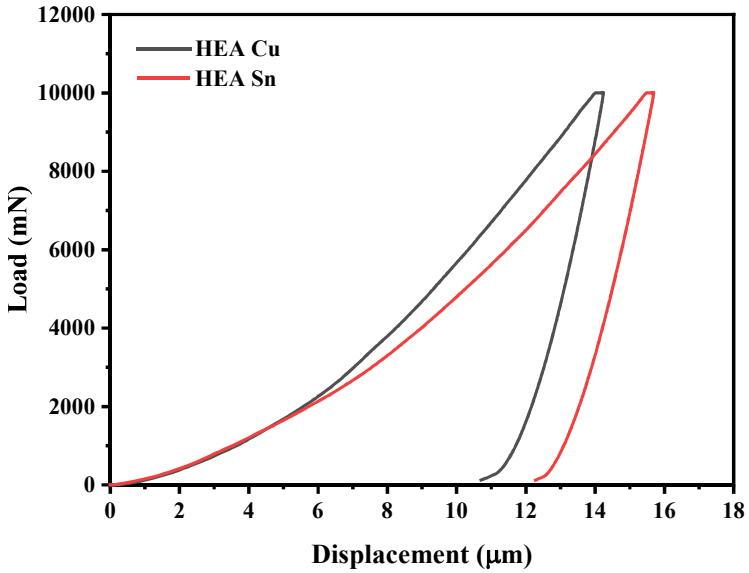

Fig. 4.30: Load displacement curve obtained for $TiNb_{1.5}Mo_{1.1}Zr_{1.15}Cu_{0.25}$ and $TiNbZr_{0.8}Mo_{0.92}Sn_{0.28}$ high entropy alloys from microindentation testing

Table 4.10: Elastic modulus of $TiNb_{1.5}Mo_{1.1}Zr_{1.15}Cu_{0.25}$ and $TiNbZr_{0.8}Mo_{0.92}Sn_{0.28}$ high entropy alloys

Sample	**$TiNb_{1.5}Mo_{1.1}Zr_{1.15}Cu_{0.25}$**	**$TiNbZr_{0.8}Mo_{0.92}Sn_{0.28}$**
Elastic modulus (GPa)	69.12	64.56

This difference can be attributed to compositional variations, which influence the atomic bonding and microstructural characteristics of the alloys. $TiNbZr_{0.8}Mo_{0.92}Sn_{0.28}$, with its tailored composition, aligns more closely with the biomechanical requirements for biomedical application.

4.5 Summary of the chapter

This chapter presents a detailed analysis of phase constitution, microstructural evolution, density, porosity, and mechanical properties of cpTi, Ti-6Al-4V, and developed Ti-based binary, ternary, and high-entropy alloys intended for biomedical implant applications. XRD and microstructural characterizations confirmed the presence of stable α and β phases in Ti-Nb alloys, with Nb effectively stabilizing the β phase. Ti-Zr alloys maintained a single α phase due to complete solid solubility between Ti and Zr, while ternary Ti-10Zr-xNb alloys exhibited a duplex α + β structure. High-entropy alloys (HEAs) displayed complex multiphase structures, BCC, orthorhombic, and tetragonal, arising from solid solution interactions and sintering-induced transformations. Microstructural features corroborated XRD results, revealing equiaxed α grains in cpTi, a biphasic α + β structure in Ti-6Al-4V, and duplex or multiphase structures in alloyed systems. Density values varied across compositions: binary Ti-Nb alloys ranged from 4.096 to 4.346 g/cm³ with 11-15% porosity, Ti-Zr alloys ranged from 4.609 to 4.885 g/cm³ with ~9% porosity, and ternary Ti-Zr-Nb alloys recorded the lowest densities (3.476-3.866 g/cm³) alongside the highest porosity (25-27%). In contrast, HEAs exhibited higher densities of 6.63 g/cm³ (HEA-Cu) and 6.41 g/cm³ (HEA-Sn) with porosities of 9% and 14%, respectively.

Hardness values significantly improved with alloying. cpTi had a hardness of 178.08 ± 11.63 HV, and Ti-6Al-4V showed 340.51 HV. Among binary alloys, Ti-10Nb (403.23 ± 21.38 HV) and Ti-10Zr (539.05 ± 27.09 HV) recorded the highest values due to solid

solution strengthening, followed by 528.78 HV for Ti-15Zr. Although hardness decreased with increased β phase (e.g., Ti-20Nb: 291.92 ± 22.52 HV), an anomalous increase was noted in Ti-25Nb (396.81 ± 12.94 HV), attributed to ω-phase formation. Ti-Zr alloys retained high hardness (e.g., Ti-5Zr: 477.59 ± 30.22 HV, Ti-15Zr: 528.78 ± 23.65 HV), exceeding that of cpTi and Ti-6Al-4V. HEAs demonstrated enhanced hardness: 470 HV (HEA-Cu) and 481 HV (HEA-Sn), owing to Mo and Sn strengthening mechanisms and dislocation hardening.

Elastic modulus trends followed β-phase stabilization behavior. Ti-20Nb showed the lowest modulus (~43 GPa), matching the modulus of human cortical bone, thus offering reduced stress shielding. Ti-Zr alloys had higher values (71-94 GPa), ternary alloys had the lowest range (30–41 GPa), and HEAs exhibited intermediate values (65-69 GPa), indicating improved biomechanical compatibility without excessive stiffness.

In conclusion, Ti-10Nb, Ti-10Zr, Ti-15Zr, and Ti-25Nb alloys outperform others within the binary and ternary groups in terms of optimized hardness and elastic modulus balance. Among all studied systems, Ti-10Nb, Ti-15Zr, Ti-10Zr-15Nb and HEA Sn offer the most promising combination of phase stability, mechanical strength, and biomechanical compatibility, making them ideal candidates for next-generation load-bearing biomedical implant applications.